Mineralogical and microstructural response of hydrated cement blends to leaching

Claudia Baldermann[1], Andre Baldermann[2†], Orkun Furat[3], Markus Krüger[1], Manfred Nachtnebel[4], Hartmuth Schroettner[4], Joachim Juhart[1], Volker Schmidt[3] and Josef Tritthart[1]

[1] Institute of Technology and Testing of Building Materials (IMBT-TVFA), Graz University of Technology, Inffeldgasse 24, 8010 Graz, Austria; e-mail: claudia.baldermann@tugraz.at, krueger@tugraz.at, joachim.juhart@tugraz.at, tritthart@tugraz.at

[2] Institute of Applied Geosciences (IAG) and NaWi Graz Geocenter, Graz University of Technology, Rechbauerstraße 12, 8010 Graz, Austria; e-mail: baldermann@tugraz.at

[3] Institute of Stochastics, Ulm University, Helmholtzstraße 18, 89069 Ulm, Germany, e-mail: orkun.furat@uni-ulm.de, volker.schmidt@uni-ulm.de

[4] Institute of Electron Microscopy and Nanoanalysis and Center for Electron Microscopy (FELMI-ZFE), Graz University of Technology, Steyrergasse 17, 8010 Graz, Austria; e-mail: manfred.nachtnebel@felmi-zfe.at, hartmuth.schroettner@felmi-zfe.at

[†] Corresponding author address:

Andre Baldermann

Institute of Applied Geosciences

Graz University of Technology

Rechbauerstraße 12, 8010 Graz, Austria

E-mail: baldermann@tugraz.at

Tel.: +43(0)316-873-6850, FAX: +43(0)316-873-7876

Keywords: Blended cements; Supplementary cementitious materials; Corrosion; Carbonation; Porosity; Pore solution; Dissolution; C-S-H

ABSTRACT

Recent advances in concrete technology have enabled the manufacturing of hydrated cements blended with high levels of supplementary cementitious materials (SCMs). These composites can exhibit mechanical and physical properties similar to ordinary Portland-based cements; yet their equivalent performance in "corrosive" environments has to be proven. In this paper, we describe mineralogical, microstructural and geochemical alteration patterns of hydrated cement pastes, despite adequate curing, containing 10 wt-% up to 70 wt-% replacement of Portland cement by SCMs, due to combined leaching and carbonation attack for 182 days. Such knowledge is highly relevant for assessing degradation features of steel-reinforced concrete in tunnels.

The dissolution of portlandite, katoite and tobermorite as well as recrystallization of C-S-H caused the development of a leached layer around the specimen`s surface. Calcite, vaterite and hydrotalcite precipitated within the altered zone, but no passivation effect due to clogging of pore space by these deposits was observed. The thickness of the altered layer, the amounts of portlandite dissolved and $CaCO_3$ phases neo-formed, the decrease in the Ca/Si molar ratio of C-S-H and the increase in total porosity were highest in pure cement paste. All hydrated cements blended with different types and levels of SCMs (including metakaolin, silica fume, limestone, granulated slag, and their combinations) have behaved better than the pure cement paste, which demonstrates the equivalent performance of these blended mixes in weakly aggressive environments.

1. INTRODUCTION

In recent times, hydrated cements blended with supplementary cementitious materials (SCMs) are widely used for the large-scale production of concrete, owning to valuable environmental, technical and economic benefits, compared to concrete made of ordinary Portland cement (OPC) [1–5]. Specifically, cement blends that are optimized with respect to the packing density and binder composition have been shown to exhibit a lower global warming potential (≥ 35 %) than OPC, while maintaining the desired workability, mechanical requirements and durability properties [5–11]. For these reasons, granulated blast furnace slag, metakaolin, fly ash and fine limestone powders among other SCMs, are nowadays substituted at different levels in concrete (e.g. 10% up to 65% for cement without other additives) [12–16]; yet the equivalent performance and durability of these mix designs in different environments (e.g. in tunnels) have to be proven.

Concrete structures are frequently subjected to different forms of physical and chemical attacks, such as leaching, carbonation, freeze-thaw and external sulfate attack [12,17–21]. Specifically, cast-in-place concrete linings, which are used in tunnels as a permanent support measure, are often exposed to so-called “soft waters”, i.e. representing poorly mineralized, natural waters (e.g. meteoric or drainage solutions) that are undersaturated with respect to (hydrated) cement phases [22]. Resultant leaching action can force the decomposition of cementitious materials and is subsequently leading to an increase of porosity and reduction of strength; thus opening the door for more deleterious attacks [19,23,24]. The response of OPC-based concrete to leaching is generally well understood; however, the (life-time) performance of hydrated cements blended with different types and levels of SCMs in weakly aggressive environments is still poorly constrained, and the mineralogical and microstructural response of such mixes to leaching not entirely understood.

It is generally accepted that the type, amount, composition and distribution of cement hydrates in the cement paste take a key control on the microstructural characteristics (total porosity,

pore size distribution etc.) and durability of the hardened concrete [22]. Hence, advanced knowledge of the hydration processes in OPC is required, which may be summarized as follows: the clinker phases, i.e. alite [Ca_3SiO_5], belite [Ca_2SiO_4], tricalcium aluminate [$Ca_3Al_2O_6$], calcium aluminoferrite [$Ca_2(Al,Fe)_2O_5$] and gypsum [$CaSO_4 \cdot 2H_2O$], typically react with water to form portlandite [$Ca(OH)_2$], calcium silicate hydrates [C-S-H], monosulfoaluminate [$Ca_4Al_2(SO_4)(OH)_{12} \cdot 6H_2O$] and ettringite [$Ca_6Al_2(SO_4)_3(OH)_{12} \cdot 26H_2O$]. In the presence of limestone (micro)fillers, monocarboaluminate [$Ca_4Al_2(CO_3)(OH)_{12} \cdot 5H_2O$], hemicarboaluminate [$Ca_4Al_2(CO_3)_{0.5}(OH)_{13} \cdot 5.5H_2O$], hydroxyl-AFm [$Ca_4Al_2(OH)_{12} \cdot 7H_2O$] or Friedel's salt [$Ca_2Al(OH)_6(Cl,OH) \cdot 2H_2O$] can also form [25–27]. Importantly, during progressive hydration, $Ca(OH)_2$ can react further with SCMs to form additional C-S-H, which represents the main reaction product in fully hydrated OPC and in hydrated cement blends. The nature, composition and quantity of C-S-H in the hardened cement paste significantly contribute to the mechanical properties (i.e. early strength development) and durability of concrete structures [25,28].

The reduction of the $Ca(OH)_2$ content in favor of C-S-H phase formation can accelerate steel corrosion, e.g. in concrete repairs and single shell concrete and shotcrete structures, whether mesh or fiber reinforced, especially in combination with leaching and carbonation [10,29–31]. Steel, embedded in concrete, is physically protected by the concrete layer itself and chemically by the thin passive layer that develops on the steel surface under highly alkaline conditions (pH $\sim\geq$ 12.5) [22,32,33]. If the $Ca(OH)_2$ content is initially reduced by the reaction with SCMs or progressively leached away from of the cement paste during interaction with soft waters, as indicated before, the pH of the pore solutions will start to decrease. Such pH drop increases the risk for the invasion of CO_2 from the atmosphere and for the uptake of dissolved inorganic carbon species from percolating groundwater; thus, speeding up the rate of carbonation front propagation from the concrete surface towards the steel reinforcement

98 [32,34–39]. These processes, if initiated once, can rapidly shift the regime from passivation to
99 steel corrosion.
100 The resistance of concrete to leaching, carbonation and steel corrosion depends mainly on the
101 binder composition and on the microstructure, which are controlled by the mix design, type of
102 cement and SCMs used, water/binder ratio, curing etc. [27,37,39,40]. Insufficient curing, for
103 example, has a direct negative effect on concrete permeability and therefore on the resistance
104 to withstand the ingress of Cl^- ions and gaseous CO_2 among other deleterious components
105 [41,42]. The effects of these variables on the durability of hydrated cement blends have been
106 extensively studied, but significant gaps in knowledge still persist regarding the mineralogical
107 and microstructural response of hydrated cement blends during interaction with soft waters. In
108 this paper, we elucidate the physicochemical controls and reaction paths leading to
109 modifications of the microstructure, mineralogy and chemical composition of hydrated
110 cement blends due to soft leaching attack.
111
112 ## 2. MATERIALS AND METHODS
113 ### 2.1 Materials, testing procedure and microstructural inspection
114 The mix design of the cement pastes is shown in Table 1. In detail, a reference cement paste
115 (CEM_{100}) made from CEM I 52.5R (mean particle diameter - d_{50} = 7.0 µm) with a clinker
116 content of >95 wt-% and C_3A content of ~12 wt-% was cast, according to [43]. Five cement
117 blends were prepared by mixing the same CEM I 52.5R with different proportions and types
118 of SCMs, such as silica fume (SF: d_{50} = 0.3 µm), metakaolin (MK: d_{50} = 2.1 µm), limestone
119 mesofiller (MEF: d_{50} = 5.0 µm), limestone microfiller (MIF: d_{50} = 1.2 µm) and granulated
120 slag (GS: d_{50} = 10.9 µm). These samples are labelled as CEM_{90}/SF_{10}, CEM_{30}/GS_{70},
121 CEM_{90}/MK_{10}, $CEM_{60}/MEF_{32.5}/MIF_{7.5}$ and $CEM_{60}/MEF_{32.5}/MK_{7.5}$, where the number indicates
122 the amount of SCM substitution by wt-% for CEM I. All specimens were fabricated at a
123 constant water/binder-ratio of 0.6 (w/b-ratio, where b denotes the sum of CEM I 52.5R as

well as latent-hydraulic GS, pozzolanic SF, MK and the two inert limestone powders, i.e., MEF and MIF). However, the portion of hydraulically active materials differed from 100 % for CEM_{100} and blends with GS, SF and MK to only 60 % for $CEM_{60}/MEF_{32.5}/MIF_{7.5}$.

Table 1. Mix design for the reference cement and cement blends (total volume: app. 460 to 470 cm³).

Sample ID	CEM I 52,5 R [cm³]	GS [cm³]	SF [cm³]	MK [cm³]	MEF [cm³]	MIF [cm³]	water [cm³]	w/b [-]
CEM_{100}	159.6						300.6	0.6
CEM_{30}/GS_{70}	47.9	120.1					300.6	0.6
CEM_{90}/SF_{10}	143.6		22.8				300.6	0.6
CEM_{90}/MK_{10}	143.6			19.3			300.6	0.6
$CEM_{60}/MEF_{32.5}/MIF_{7.5}$	95.7				60.3	13.9	300.6	0.6
$CEM_{60}/MEF_{32.5}/MK_{7.5}$	95.7			15.2	60.3		300.6	0.6

The cement pastes were filled in plastic bags, which were placed in cylindrical plastic tubes (diameter of 70 mm, height of 150 mm) and rotated over night to prevent segregation. Then, the bags were extracted from the tubes, placed in a second plastic bag and stored at 20°C (Fig. 1). During sample storage, the specimen`s surface was sporadically coated with a thin layer of bleed water due to an interfacial zone that developed between the plastic bag and the paste (i.e. ~100 % relative humidity was maintained in the second plastic bag). Noteworthy, the bleed water and the pore solutions were undersaturated with respect to the partial pressure of CO_2 in atmosphere ($P_{CO2} = 10^{-3.4}$ atm) at any time during curing, allowing atmospheric CO_2 to diffuse through the semi-permeable plastic bags, where it was converted into dissolved carbon species (mainly CO_3^{2-}, Fig. 1). In the literature, such storage conditions are often described as ideal, i.e. reducing the self-desiccation in the cement paste and keeping the material water-saturated or nearly water-saturated as long as possible in order to produce fully hydrated and hardened cement pastes without any optical signs of alteration [44,45]. Several studies [41,42] have concluded that curing is crucial for concrete (esp. with pozzolanic material) to improve its corrosion resistance, and that inadequate curing will result in poor performance.

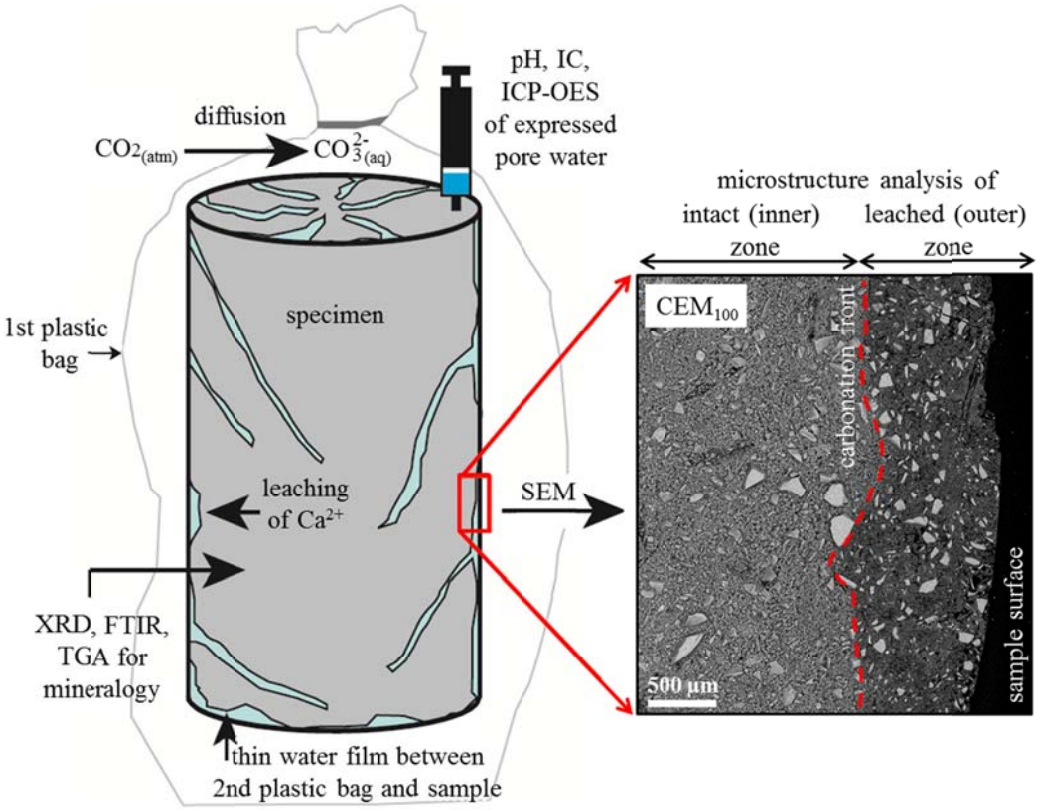

Fig. 1. Schematic representation of the test procedure and multi-methodological approach used in this study.

After 28, 56, 91 and 182 days of storage in plastic bags, the packing was removed and the test specimen were placed into a steel cylinder of a special adapted hydraulic press, which squeezes the samples with a maximum load of 1300 kN/mm^2 [46,47]. The expressed pore solutions (~1-5 mL) were separated by a syringe and filtered through 0.45 µm cellulose acetate membranes in preparation for subsequent chemical analyses.

For mineralogical and chemical analysis only the samples after 182 days were used and dried in an oven at 80 °C (Bonnet & Balayssac, 2018) for less than 2-3 h in order to avoid thermal alteration and recrystallization of the hydrated cement phases, and then crushed in jaw crusher. Afterwards, the specimens were subjected to visual inspection: all samples showed a modified outer zone and an intact inner zone (Fig. 1), with a thickness of the alteration layer depending mainly on the paste composition. For this reason, three types of sub-samples were considered for the further solid-phase analyses. The first sub-sample having a size of app. 4.5 x 0.7 cm from the surface to the inner zone was prepared for microstructural analyses (see

158 Fig. 1 for leached layer in CEM_{100}). The second one was divided into two sub-fractions,
159 namely the altered outer zone and the unaltered inner zone of the specimen, respectively,
160 which were separated by a conventional micro-drill. The latter sub-samples were finely
161 ground in a ball mill for 10 min in preparation for subsequent mineralogical analyses.
162

163 **2.2 Analytical methods**

164 *2.2.1 Solid-phase characterization*

165 The mineralogical composition of the altered and unaltered samples was determined by X-ray
166 diffraction (XRD) of random oriented powder preparations using a PANalytical X'Pert PRO
167 diffractometer equipped with a Co-radiation source (40 kV, 40 mA), 0.5° antiscattering and
168 divergence slits and a Scientific X'Celerator detector. The preparations were examined in the
169 range from 5-50° 2Θ range with a step size of 0.004° 2Θ and a count time of 40 s per step.
170 Mineral identification was realized with the PANalytical X'Pert HighScore software (version
171 2.2e) and a pdf-4 database, without consideration of the amorphous phase content [48].
172 Mid-infrared spectra (MIR) were obtained for further identification of the cement hydrates, as
173 most of these phases are “invisible” by XRD due to their low crystallinity and poorly ordered
174 structure. Therefore, Fourier-transform infrared spectroscopy (FTIR) data was obtained on a
175 PerkinElmer Frontier spectrometer using the attenuated total reflectance (ATR) configuration.
176 The spectra were recorded in the 4000-650 cm^{-1} range with a point resolution of 2 cm^{-1}.
177 The proportions of $Ca(OH)_2$ and $CaCO_3$ in altered and unaltered pastes were determined by
178 thermogravimetry (TG) and differential scanning calorimetry (DSC) analysis performed on a
179 PerkinElmer STA 8000 thermobalance apparatus. About 30 mg of each sample powder was
180 equilibrated at ~60 % relative humidity and then heated from 30 ºC to 1000 ºC at a constant
181 heating rate of 10 °C/min under N_2 flow. Mineral quantification was realized by evaluation of
182 the TG-curves using the Pyris^{TM} software package and considering the sample-specific weight
183 losses at 450-500 °C for portlandite and at 600-800 °C for carbonates, respectively.

The microstructural characteristics (i.e. microfabrics, total porosity and chemical composition of the cement paste) of the (un)altered parts of each mix were obtained from polished sample surfaces. Observations using backscattered electrons (BSE) were made on a Zeiss Sigma 300 VP scanning electron microscope (SEM) operated at an accelerating voltage of 15 kV. This instrument is equipped with a thermal field emission gun, a solid-state BSE detector and an Oxford Instrument X-max^{80} SDD EDXS (energy dispersive X-ray spectroscopy) detector for elemental analysis, which was used for mineral identification and quantification of the Ca/Si and Al/Si molar ratios of C-S-H. BSE images of 50 μm width and 35 μm height were taken across the (un)altered zones (8-10 for each zone) of each sample to obtain a representative picture of the microstructure. In order to analyze the pore space depicted in these images quantitatively, several image pre-processing steps were applied. Firstly, noise reduction was performed with the non-local means denoising algorithm [49] using the implementation provided by the Avizo software. Secondly, segmentation of the images into pores and solids was made via a global thresholding, i.e. in the resulting binary images the pores and the solids are visualized as black and white regions, respectively. Thirdly, since the interfaces between the two phases were still rough and noisy, binary images were smoothed using morphological closing [50], with a disc of radius 0.04 μm in Matlab. Finally, from these binary images the total porosities of (un)altered zones of each sample were computed, i.e. the areas of all "black objects" in the binary images were summed up and related to the total area of the images to obtain the porosity, that is, the area fraction of pores (see Fig. S1). Median values and median absolute deviations of the porosity for each scenario were calculated (based on 8-10 images per sample) in order to quantify the variability of the porosity. In addition, the area equivalent diameters were computed for every pore cross-section depicted in the image data to characterize the smallest pores: the 1-quantiles (i.e. the value for which 1 % of the computed pore diameters are smaller) of pore diameters lie between 27 nm – 100 nm for all considered scenarios, thus making direct comparison of the microstructure of all samples possible.

210 *2.2.2 Fluid-phase characterization*

211 The expressed and filtered pore solutions were analyzed for their pH value and major, minor
212 and trace elemental concentrations. The pH of the pore solutions was measured with a WTW
213 Multi 350i pH-meter equipped with SenTix41 electrode, which was calibrated against NIST
214 buffer standard solutions at pH 7.00 and 10.00. The analytical precision of pH measurements
215 was ± 0.12 pH units at pH ≥ 13.00, as determined by replicate analyses of the samples. The
216 chemical composition of the pore solutions was analyzed in replicates with a Dionex ICS-
217 3000 ion chromatograph (IC: Na, K, Ca, SO_4, Cl) and a PerkinElmer Optima 8300 inductively
218 coupled plasma optical emission spectrometer (ICP-OES: Al, Mg, Si) with an estimated
219 accuracy of ± 3 % and ± 5 % for IC and ICP-OES analyses [51], respectively.
220 For the calculation of the concentrations of OH^- and CO_3^{2-} ions, ion charge balance, aqueous
221 speciation, ionic strength and saturation indices (SI) of the pore solutions with respect to the
222 relevant mineral phases, the PHREEQC software code (version 3.1.5-9133; [52]) in
223 combination with the CEMDATA18 thermodynamic database [53] was used. The following
224 mineral phases were taken into further consideration: portlandite, calcite, C-S-H (i.e. jennite
225 $C_{1.67}SH_{2.1}$-type and tobermorite $C_{0.83}SH_{1.3}$-type), (mono/hemi)carboaluminate,
226 monosulfoaluminate, Si-bearing hydrogarnet (katoite-type), hydrotalcite (i.e. a magnesium
227 aluminium carbonate hydrate that is typically found in slag-blended cements) and ettringite,
228 because of their high relevance (e.g. chemical reactivity) in pure cement paste and hydrated
229 cement blends subjected to leaching and carbonation.
230

231 **3. RESULTS AND DISCUSSION**

232 **3.1 Pore water geochemistry**

233 The chemical compositions of the pore solutions expressed after 28, 56, 91 and 182 days of
234 reaction time are displayed in Table S1, and important parameters plotted in Fig. 2. It is
235 evident that all pore solutions had a K-Na-OH-type composition, independent from the curing

time and original mix design used (Table 1). The OH^- ion concentration and thus the pH of the pore solutions decreased with increasing cement substitution by SCMs, as it can be seen by comparison of CEM_{100} (pH ~13.5) with the other hydrated cement blends (pH 13.0 to 13.3). However, the $[Cl^-]/[OH^-]$ ratio – a measure for the aggressivity of the pore solutions for corrosion – of CEM_{100} (0.027), CEM_{30}/GS_{70} (0.030) and $CEM_{60}/MEF_{32.5}/MK_{7.5}$ (0.030) was rather similar. In the case of CEM_{90}/MK_{10} the ratio of $[Cl^-]/[OH^-]$ was lower (0.017), compared to the reference mix. $CEM_{60}/MEF_{32.5}/MIF_{7.5}$ and CEM_{90}/SF_{10} revealed higher $[Cl^-]/[OH^-]$ ratios of 0.047 and 0.103, respectively. Note here that the critical $[Cl^-]/[OH^-]$ molar ratio indicated for corrosion risk is 0.6 for a reinforced concrete structures exposed to the atmosphere [54].

This observation matches with findings of Rasheeduzzafar et al. [55], who have shown that the $[Cl^-]/[OH^-]$ ratio of hydrated cements blended with 10 % and 20 % of microsilica can be more than doubled, due to the consumption of OH^- ions during cement hydration. However, based on accelerated corrosion tests (exposure to 5 % NaCl solution) these authors have concluded that elevated $[Cl^-]/[OH^-]$ratios in the pore solutions do not negatively affect the start of corrosion (i.e. the initiation time) and hence the material`s performance. This may be related to the densification of the cement paste by the pozzolanic reaction between microsilica and $Ca(OH)_2$ [55]. From these results it can be inferred that the resistance of hydrated cement blends against corrosion cannot be determined by a certain parameter of the pore solution, like the $[Cl^-]/[OH^-]$ ratio or a critical threshold Cl^-content, and that other factors of influence, e.g. oxygen availability and aqueous species have to be considered.

Indeed, exposure of pastes to poorly mineralized waters that are undersaturated with respect to dissolved inorganic carbon species represents a leaching scenario (Fig. 1), which is highly relevant for reinforced concrete structures [19]. This is because the boundary conditions used in this test procedure resemble to those often found in tunnels, such as high relative humidity, undersaturation with respect to the CO_2 concentration in air, low to ambient temperature,

interaction with soft waters, etc. [22,47]. Specifically, in consequence of CO_2 absorption from the tunnel atmosphere by the alkaline pore solutions developing in concrete, and the subsequent hydroxylation of $CO_{2(aq)}$ with OH^- ions, both the dissolution of $Ca(OH)_2$ and the crystallization of anhydrous calcium carbonates, such as calcite, aragonite and vaterite [$CaCO_3$ polymorphs], are promoted [32].

As expected, the aqueous CO_3^{2-} concentration remained near-constant at 46 ± 6 mg/l for all mixes, suggesting continuous uptake of atmospheric CO_2 into the alkaline pore solutions. Such constant supply of CO_3^{2-} ions is important for the corrosion development of hydrated cement blends, because during carbonation the $Ca(OH)_2$ content originally present in the paste is progressively consumed in favor of calcite and AFm phase formation. Coincidently, the pH of the pore solution will start to decrease, from initial pH values of > 12-13 down to < 8 in severely carbonated pastes [19,32,56]. In the present case, the expected drop in pH over time was counterbalanced by the continuous leaching of $Ca(OH)_2$ and alkali hydroxides (~5-16 g/l of Na^+ and K^+) from the cement paste, which prevented the samples from severe corrosion. This effect is more pronounced in CEM_{100}, which has the highest $Ca(OH)_2$ content among all other samples, as the cements blended with SCMs started consuming some of the $Ca(OH)_2$ already during hydration, in favor of C-S-H formation [22]; thus slightly reducing the system-inherited pH-buffering capacity (Table S1). Besides, elevated concentrations of aqueous Mg^{2+} (1-10 mg/l), Ca^{2+} (20-179 mg/l), Al^{3+} (2-70 mg/l), SO_4^{2-} (28-751 mg/l) and Si^{4+} ions (10-147 mg/l) in the pore solutions of all mix designs suggest (intense) chemical modifications of the cement paste, although the individual element profiles revealed no systematic variations with time (Fig. 2a-d). It is clear that the concentration range of these elements measured in the pore solutions is mainly controlled by the interplay between the dissolving cement clinker phases and subsequently precipitating cement hydrates in each mix.

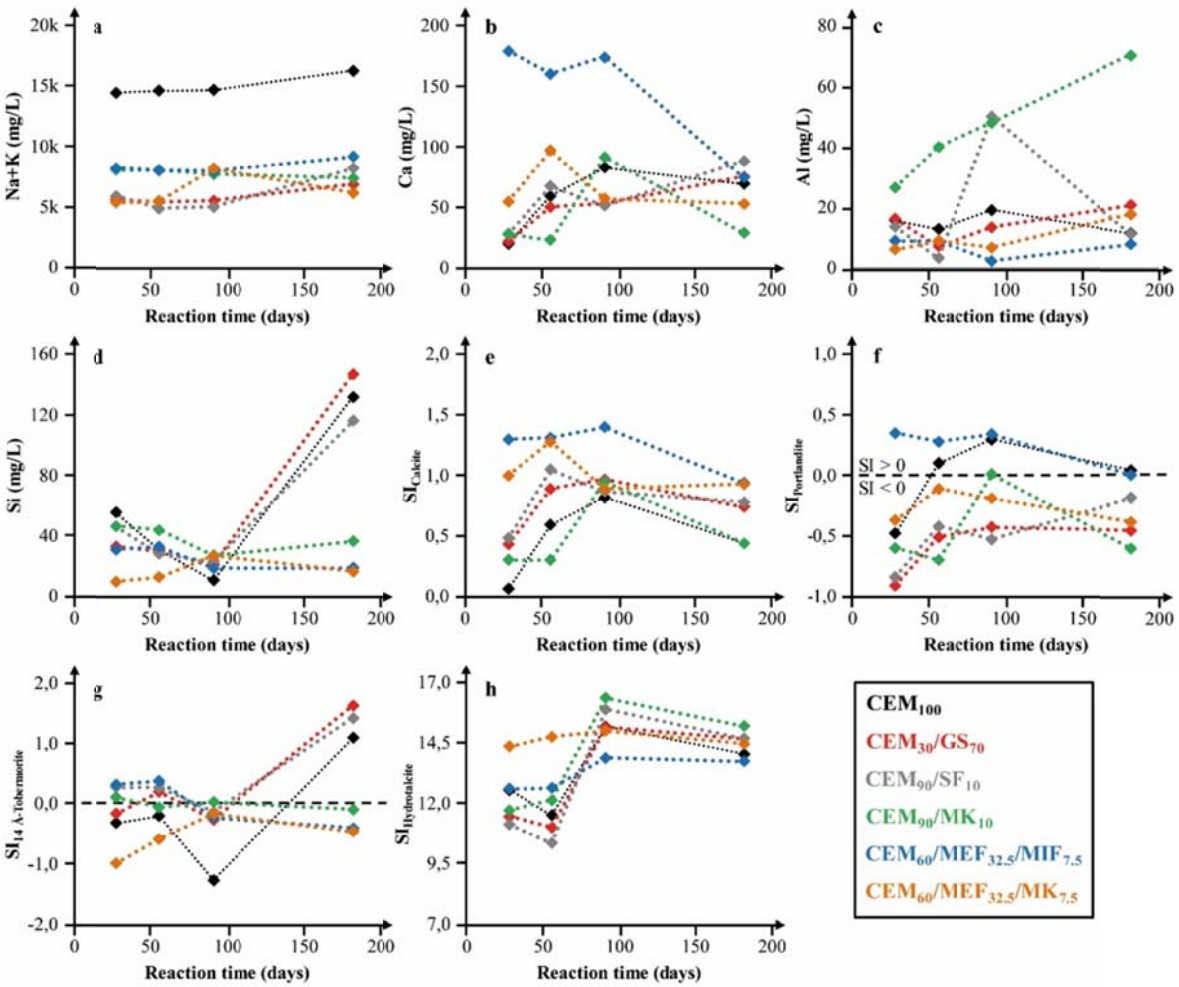

Fig. 2. Temporal evolution of the chemical composition of the pore solutions expressed from cement blends after certain reaction times. Plots are shown for selected elements (K+Na, Ca, Al, Si) and for saturation indices (SI) of portlandite, calcite, tobermorite and hydrotalcite. SI < 0 indicates dissolution; SI > 0 indicates precipitation.

The results of hydrochemical modelling (Fig. 2 and Table S1) indicate that all pore solutions were close to saturation or slightly undersaturated with respect to portlandite and tobermorite (i.e. SI values < 0 indicate mineral dissolution), but they were dominantly supersaturated with respect to $CaCO_3$ polymorphs, siliceous hydrogarnet (katoite), (mono/hemi)carboaluminate, ettringite, jennite, monosulfoaluminate and hydrotalcite (i.e. SI values > 0 indicate mineral precipitation) after 182 days (Fig. 2f-h). Therefore, one would expect significant changes in the mineralogical composition and microstructure of the hydrated cement blends after curing in weakly aggressive environment (see sections below for further discussion).

298 **3.2 X-ray diffraction**

299 XRD patterns obtained from unaltered versus altered samples are shown in Fig. 3. The
300 unaltered materials comprised of minor amounts of belite, high amounts of cement hydrates
301 and varying contents of calcite, dolomite and quartz. Portlandite and C-S-H were the most
302 abundant hydration products in all mixes. High amounts of primary calcite were found in the
303 mixes $CEM_{60}/MEF_{32.5}/MIF_{7.5}$ and $CEM_{60}/MEF_{32.5}/MK_{7.5}$, reflecting the mix design (Table 1).
304 The siliceous hydrogarnet group mineral katoite [$Ca_3Al_2(SiO_4)_{0.8}(OH)_{8.8}$] was more abundant
305 in the samples CEM_{90}/MK_{10} and $CEM_{60}/MEF_{32.5}/MK_{7.5}$, due to additional supply of reactive
306 silica from the MK additives [57–59]. The mix CEM_{30}/GS_{70} developed by far the highest
307 contents of hydrotalcite [$Mg_6Al_2CO_3(OH)_{16}\cdot 4(H_2O)$] and of other AFm phases, which is
308 typical for cement blended with slag [60]. The presence of Friedel's salt cannot be excluded
309 in these mixes, as its main reflection overlaps with the peaks of other AFm phases, and since
310 this phase is known to form solid solutions with some AFm phases [20]. Similarly, vaterite
311 could be barely present in all mixes, though its main reflections (011 and 012) are poorly
312 developed and partly overlap with those of belite ($20\overline{2}$ and $02\overline{2}$). The presence of 9 Å-
313 tobermorite in the unaltered samples results from drying at 80 °C, rather than indicating
314 incomplete cement hydration, as 14 Å-tobermorite [$Ca_5Si_6O_{16}(OH)_2\cdot 7H_2O$] forms during wet
315 storage [61–63].

316 In contrast, katoite and tobermorite were absent in the altered samples, and the portlandite
317 peaks significantly lost intensity (Fig. 3), which suggests dissolution of these mineral phases.
318 The reflections of calcite (± vaterite) and hydrotalcite have gained intensity, which points to
319 the accumulation of these phases in the altered zone, confirming the hydrochemical modelling
320 results (Table S1). However, it is worthy to note that portlandite, tobermorite, hydrotalcite and
321 katoite among others are quantitatively consumed during carbonation. This indicates that the
322 carbonation reaction has not been fully completed after 182 days of reaction time [59],
323 probably reflecting the "mild" exposure conditions used in this research. Also, the neo-

formation of ettringite was not observed in all mixes, despite of potentially favorable formation conditions (Table S1).

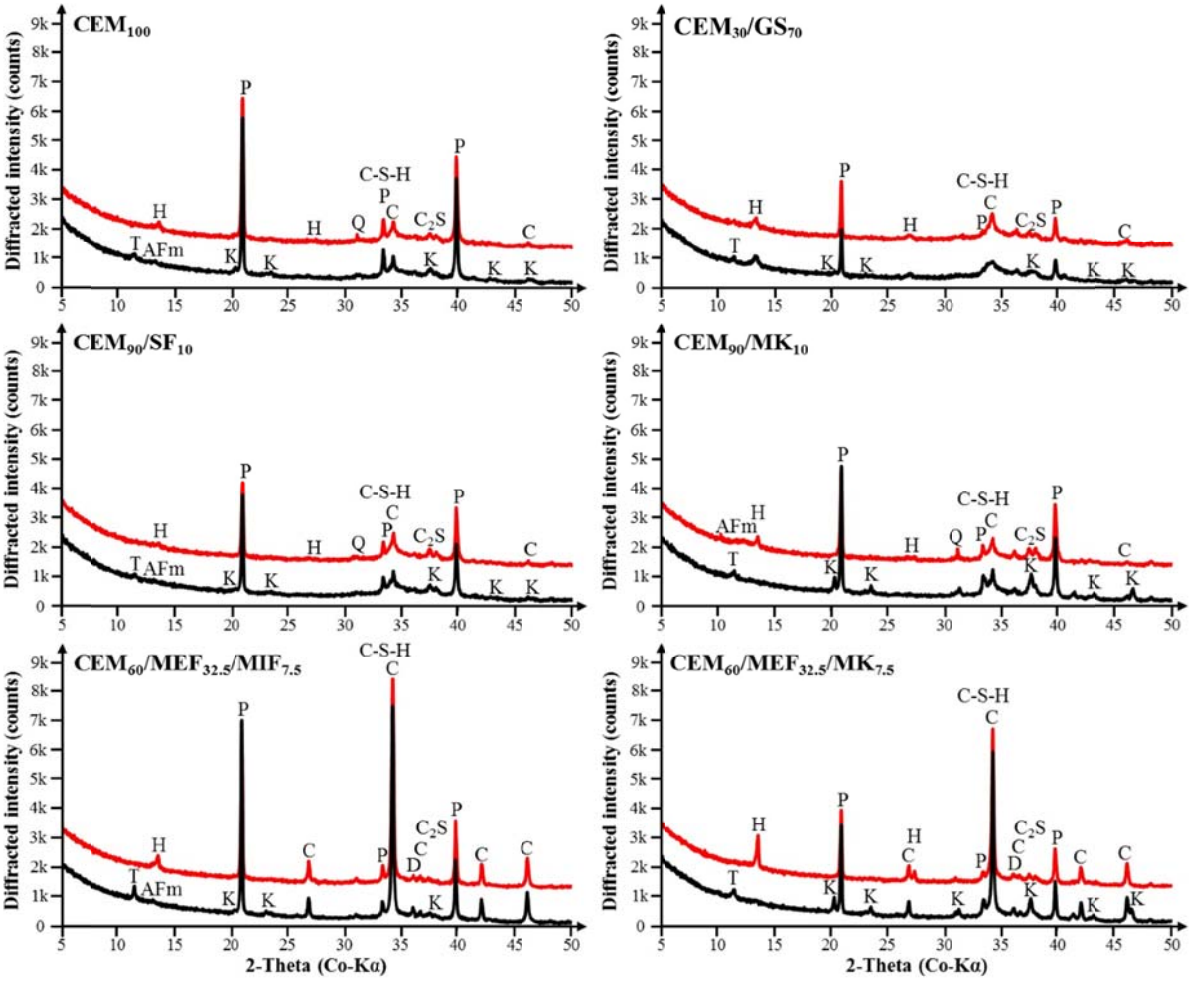

Fig. 3. XRD patterns of hydrated cement blends after curing for 182 days (black and red curves correspond to unaltered and altered samples, see Fig. 1). T – 9 Å-tobermorite, AFm –calcium aluminate hydrate, H – hydrotalcite, P – portlandite, K – katoite, C – calcite, C-S-H – calcium silicate hydrate, D – dolomite, C_2S – belite.

Similar alteration patterns have been observed in cements blended with alkali activated blast-furnace slag pastes, i.e. tobermorite and katoite progressively transformed into hydrotalcite, thereby inducing microstructural damage to the cement matrix [64–66]. Bernal et al. [59] have proposed that the rate of this reaction strongly depends on the CO_2 concentration, as it directly affects the pH of the pore solutions and related alkali carbonate/bicarbonate phase equilibria.

Given the relatively low CO_2 concentration in air (~400 ppm), the carbonation reactions mentioned before should be slow, compared to accelerated systems applying app. 2 to 4 % of CO_2, but similar to those observed in tunnel environments [22]. Future research is needed to constrain the relations between mineral phase reactivity, alteration mineralogy and corrosion behavior of hydrated cement blends exposed to CO_2 environments.

3.3 Infra-red spectroscopy

MIR spectra of samples taken from the unaltered versus altered zone of the test specimens are shown in Fig. 4. The presence of portlandite in all sample types is indicated by an IR band at 3643 cm^{-1}. Very broad and weak double peaks at ~1000 cm^{-1} and ~900 cm^{-1} (Si-O asymmetric stretching vibrations) correspond to traces of belite [67,68]. Adsorption at 872 cm^{-1} and 712 cm^{-1} (asymmetrical/symmetrical deformation vibrations of CO_3^{2-}) is related to occurrences of calcite in all samples. The relative increase in intensity of the 1421 versus 1477 cm^{-1} band (asymmetrical stretching of CO_3^{2-}) in the altered samples suggests a shift towards decreasing particle sizes and surface roughness of secondary calcite and vaterite that form due to CO_2 ingress through the plastic bag wall [56,69]. The adsorption centered at ~3400 cm^{-1} and 1639 cm^{-1} is related to OH^- stretching modes and H-O-H bending modes in various hydroxyl groups and in surface-bound water [70]. The weak adsorption at 2982 cm^{-1} is due to the presence of trace amounts of ethanol remaining in the solids from preparation (C-H stretching vibration, [16]). The IR band at 1371 cm^{-1} (asymmetrical stretching of CO_3^{2-}) is assigned to hydrotalcite and AFm phases in all samples [71]. This IR band is more pronounced in CEM_{30}/GS_{70} due to high amounts of hydrotalcite in this mix (Fig. 3). Adsorption at 3748 cm^{-1}, 1115 cm^{-1} and in the range between 1200 and 800 cm^{-1} refers to Si-O-Si and Si-O-Al stretching vibrations in tobermorite, katoite and poorly crystallized C-S-H [72,73].

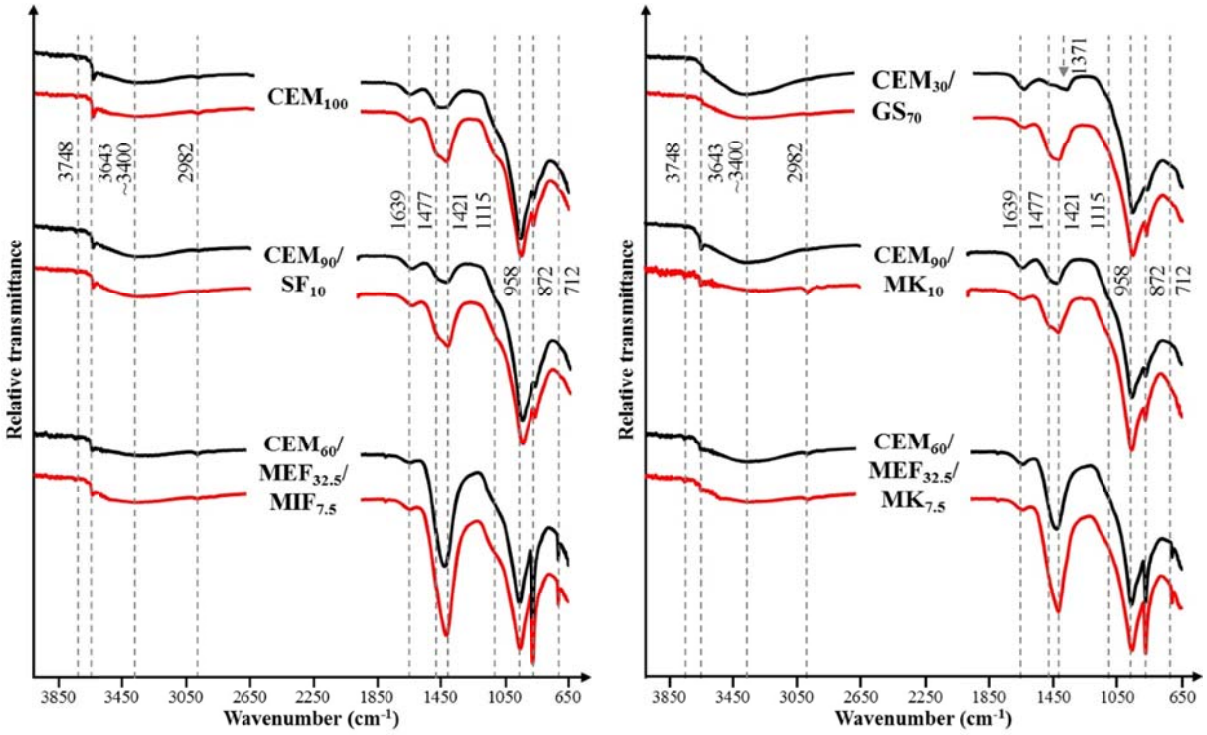

360

361 **Fig. 4.** FTIR patterns of hydrated cement blends after hardening in plastic bags for 182 days (black and red
362 curves correspond to unaltered and altered samples, see Fig. 1).

363 The main adsorption shifted from ~960 cm^{-1} to ~950 cm^{-1} for C-S-H from the unaltered and
364 altered zone of each sample, independent for the original mix design used. This systematic
365 decrease towards lower wavenumbers suggests intense modifications of the C-S-H structure
366 due to progressive calcium leaching and related recrystallization. Such alteration patterns are
367 typically associated with (i) decreasing polymerization of the tetrahedral chains of C-S-H, (ii)
368 substitution of Si-O-Si by Si-O-Al bonds and (iii) lowering of the Ca/Si ratio in the C-S-H
369 structure [74]. These processes are further seen by an increase in intensity of the ~1100 cm^{-1}
370 band of C-S-H in the altered zone, which is assigned to abundant structural defects (Fig. 4). In
371 terms of corrosion, calcium-depleted and highly defect (tobermorite-type) C-S-H should have
372 a higher solubility than the calcium-rich (jennite-type) counterparts [75], thus affecting the
373 chemical reactivity of the paste.

374 **3.4 Thermogravimetric analysis (TGA)**

375 The TG- and DSC-curves of samples taken from the altered versus unaltered zones of the
376 hydrated cement blends and reference mix exhibited a strong weight loss (-5.0 to -12.9 wt-%)
377 between 30 °C and 200 °C (i.e. the main peak was located at ~130-140 °C) and a second
378 moderate one between 450 °C and 500 °C (-1.4 to -5.7 wt-%). Another relatively weak weight
379 loss was observed between 600 °C and 670 °C (-1.1 to -3.8 wt-%) and a fourth weak to strong
380 one (-0.3 to -14.4 wt-%) between 670 °C and 800 °C. The DSC-signal revealed in all cases
381 negative excursions, which is indicative of endothermic reactions. Hence, these weight losses
382 have been attributed to the removal of H_2O and CO_2 molecules from C-S-H and AFm phases
383 (< 200 ºC), dehydroxylation of portlandite (~480 °C) and decomposition of vaterite (< 670
384 °C) and calcite (670-800 °C), respectively [76]. Accordingly, the weight losses obtained in
385 these temperature ranges are tabularized in Table 2, together with changes in the $Ca(OH)_2$ and
386 $CaCO_3$ contents upon leaching and carbonation, for all samples. It should be noted that we
387 cannot report absolute contents for C-S-H, because of formation of multi-phase products
388 (tobermorite, hydrotalcite and AFm, katoite etc.) and potential modifications of the water
389 content of tobermorite induced during sample curing and drying (i.e. presence of 9 Å-
390 tobermorite instead of 14 Å-tobermorite).

391 The portlandite content was reduced and the C-S-H phase content was increased in hydrated
392 cements substituted with GS, SF and MK, compared to CEM_{100}, due to consumption of
393 $Ca(OH)_2$ during hydration of SCMs [25,28]. However, the $CaCO_3$ content in these mixes was
394 relatively similar (1.4 to 2.5 wt-%). $CEM_{60}/MEF_{32.5}/MIF_{7.5}$ and $CEM_{60}/MEF_{32.5}/MK_{7.5}$
395 displayed much lower C-S-H and $Ca(OH)_2$ contents, but a high $CaCO_3$ content, which reflects
396 the high level of limestone substitution for cement in these mixes (Table 1) and the low
397 reactivity of carbonate fillers during cement hydration [12,77].

Table 2. Compilation of weight losses of C-S-H, portlandite (P), vaterite (V) and calcite (C) within the hydrated cement blends as a function of mix design approach (unaltered zones) and exposure to calcium leaching and carbonation (altered zone), based on TGA data. Variations in the quantitative phase contents of portlandite and secondary calcium carbonates (Carb) are given as Δ-values (calculated by the difference of mineral abundances in the unaltered and altered zones). Note the imbalance in the calcium budget between reaction educts and products for all samples (Fig. 5d). See text for further explanations.

Sample ID	Position of sample	C-S-H† wt-%	P wt-%	V wt-%	C wt-%	Δ-P wt-%	Δ-Carb wt-%
CEM_{100}	unaltered zone	8.1	5.7	1.3	0.8		
CEM_{100}	altered zone	7.7	4.5	1.7	3.8	-5.1	6.7
CEM_{30}/GS_{70}	unaltered zone	12.9	1.4	1.1	0.3		
CEM_{30}/GS_{70}	altered zone	6.8	1.5	2.1	1.7	0.2	3.1
CEM_{90}/SF_{10}	unaltered zone	12.0	3.6	1.2	0.8		
CEM_{90}/SF_{10}	altered zone	8.6	3.3	1.9	2.3	-1.4	3.3
CEM_{90}/MK_{10}	unaltered zone	12.2	3.4	1.6	0.8		
CEM_{90}/MK_{10}	altered zone	9.1	3.1	3.0	0.6	-1.1	-0.4
$CEM_{60}/MEF_{32.5}/MIF_{7.5}$	unaltered zone	5.0	3.8	2.8	13.9		
$CEM_{60}/MEF_{32.5}/MIF_{7.5}$	altered zone	5.2	3.5	3.5	14.4	-1.2	1.0
$CEM_{60}/MEF_{32.5}/MK_{7.5}$	unaltered zone	8.4	2.1	2.5	11.7		
$CEM_{60}/MEF_{32.5}/MK_{7.5}$	altered zone	7.5	1.9	3.8	11.5	-0.6	-0.5

†refers to the volatile content of all hydrated cement phases (i.e. weight loss in the temperature range from 30 °C to 200 °C)

A reduction in the volatile content of C-S-H (Table 2), a strong loss in the portlandite content (Fig. 5a) and a sudden increase in the amounts of neo-formed vaterite (Fig. 5b) and calcite (Fig. 5c) were evident by comparison of samples collected from the altered and unaltered zone of each mix. CEM_{100} showed by far the highest decrease in the portlandite content and the highest increase in the carbonate content, compared to the hydrated cement blends (Table 2), which suggests an outstanding performance of the blends in terms of protection of reinforcement (see section on microstructure for further evaluation).

Importantly, stoichiometric considerations of the calcium budget (defined as Δ-Ca) yielded an imbalance for all mixes: there is much more calcium associated with the secondary carbonates than it could have been theoretically provided by the dissolution of portlandite (i.e. all values plot below the 1:1 line for Δ-Ca in Fig. 5d). For example, in CEM_{100} one can see a loss of -5.1

wt-% of portlandite and a gain of +7.6 wt-% of calcite, which is equivalent to a Δ-Ca excess of ~39 % in the alteration zone (Table 2). This finding documents the reactivity of hydrated cement phases even under highly alkaline conditions (pH ≥ 13.0, Table S1), i.e. it is suggested that leaching of tobermorite, katoite, etc. provided an important fraction of Ca^{2+} ions to the pore solutions to be used for the subsequent formation of $CaCO_3$ polymorphs.

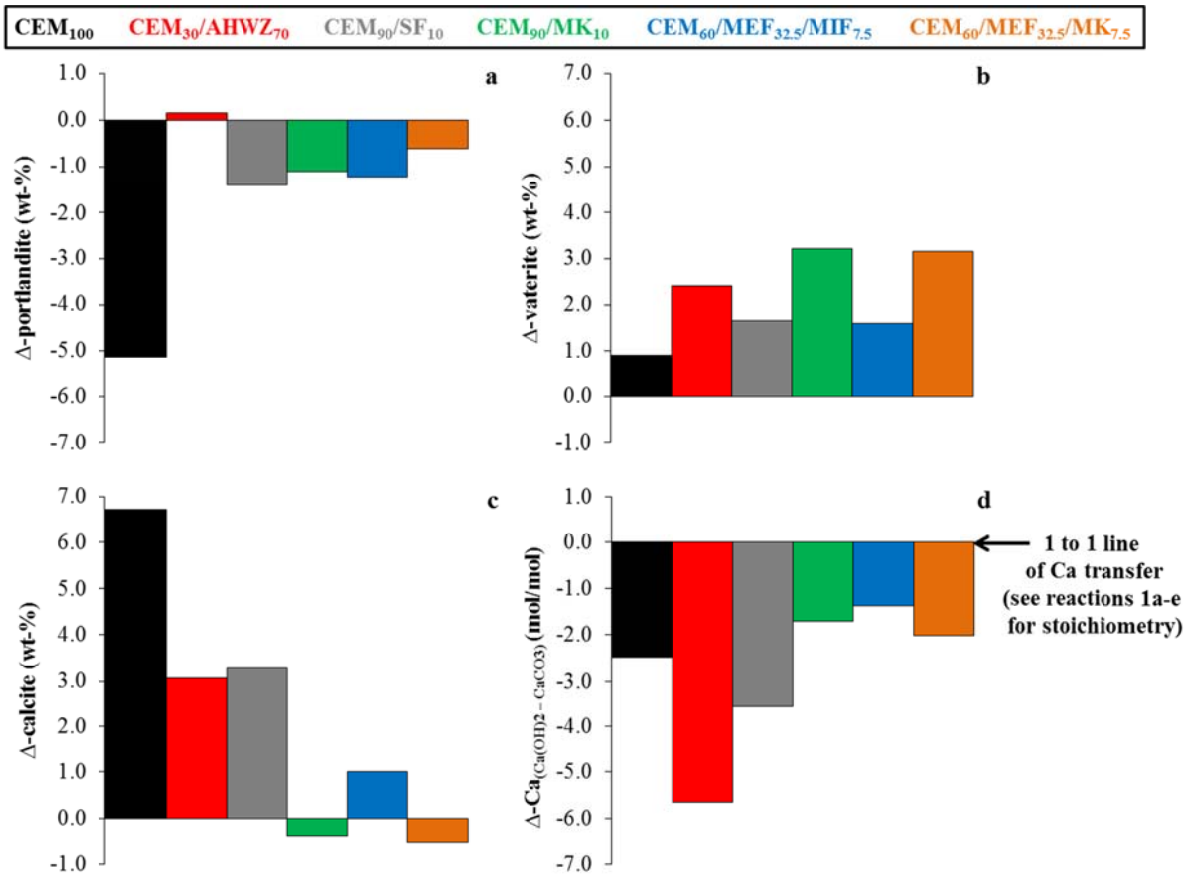

Fig. 5. Change in the portlandite (a), vaterite (b) and calcite (c) content of hydrated cement blends after curing in weakly aggressive environments. Negative values indicate mineral dissolution; positive values indicate mineral neo-formation. Note the imbalance in the calcium budget between the ideal dissolution portlandite and formation of calcite+vaterite (reported as Δ-Ca ratio in d, where the stoichiometric reaction is indicated by the 1 to 1 line), which is counterbalanced by calcium leaching from C-S-H.

3.5 Microstructure analysis (SEM)

3.5.1 Evaluation of alteration patterns

Alteration features within CEM_{100} are displayed in Figure 6. From the BSE image sequences (Fig. 6a-f) and EDX spectra of C-S-H collected from the unaltered and altered zones (Fig. 6g) one can see significant microstructural, mineralogical and geochemical modifications of the cement paste due to leaching, which are described in detail below (note that all other samples blended with SCMs were evaluated in this way).

The corrosive layer of CEM_{100} had a thickness of 1470 ± 220 µm, as it is indicated by 30 replicate measurements across the entire sample surface (Fig. 6a). The boundary between the unaltered and altered zone is marked by an extremely thin transition zone (e.g. the interfacial transition zone is less than 100 nm thick in Fig. 6a-b), reflecting the onset of leaching and carbonation [15,19,20]. In the inner parts of CEM_{100}, portlandite and more rarely belite occurred as isolated grains within the very dense C-S-H matrix (total porosity: 9.5 ± 2.0 %, Fig. 6c). In the outer parts, belite and portlandite were leached away or were passivated by a thin calcite layer (Fig. 6d and reaction 1), which prevented these phases from further dissolution [22].

A strong increase in the total porosity to about 23.1 ± 7.0 % was evident in the altered zone of CEM_{100}, which is related to (i) dissolution of cement clinker phases and portlandite (Fig. 6d), (ii) alteration of tobermorite, AFm phases and katoite into hydrotalcite (Fig. 3) and (iii) calcium leaching and recrystallization of C-S-H (Fig. 4). The latter is seen by a decrease in the Ca/Si molar ratio, from 1.71 ± 0.20 to 1.23± 0.21, and an increase in the Al/Si molar ratio, from 0.12 ± 0.05 to 0.24 ± 0.09, of C-S-H from the unaltered versus altered zones (Fig 6g). The SEM-EDX data further revealed a very low Na content (≤ 0.2 wt-%) and a low Mg content (0.5-1.3 wt-%) of C-S-H from CEM_{100}, which implies that sodium aluminosilicate hydrates (N-A-S-H) and magnesium aluminosilicate hydrates (M-A-S-H) did not form to a great extent in this mix [78,79].

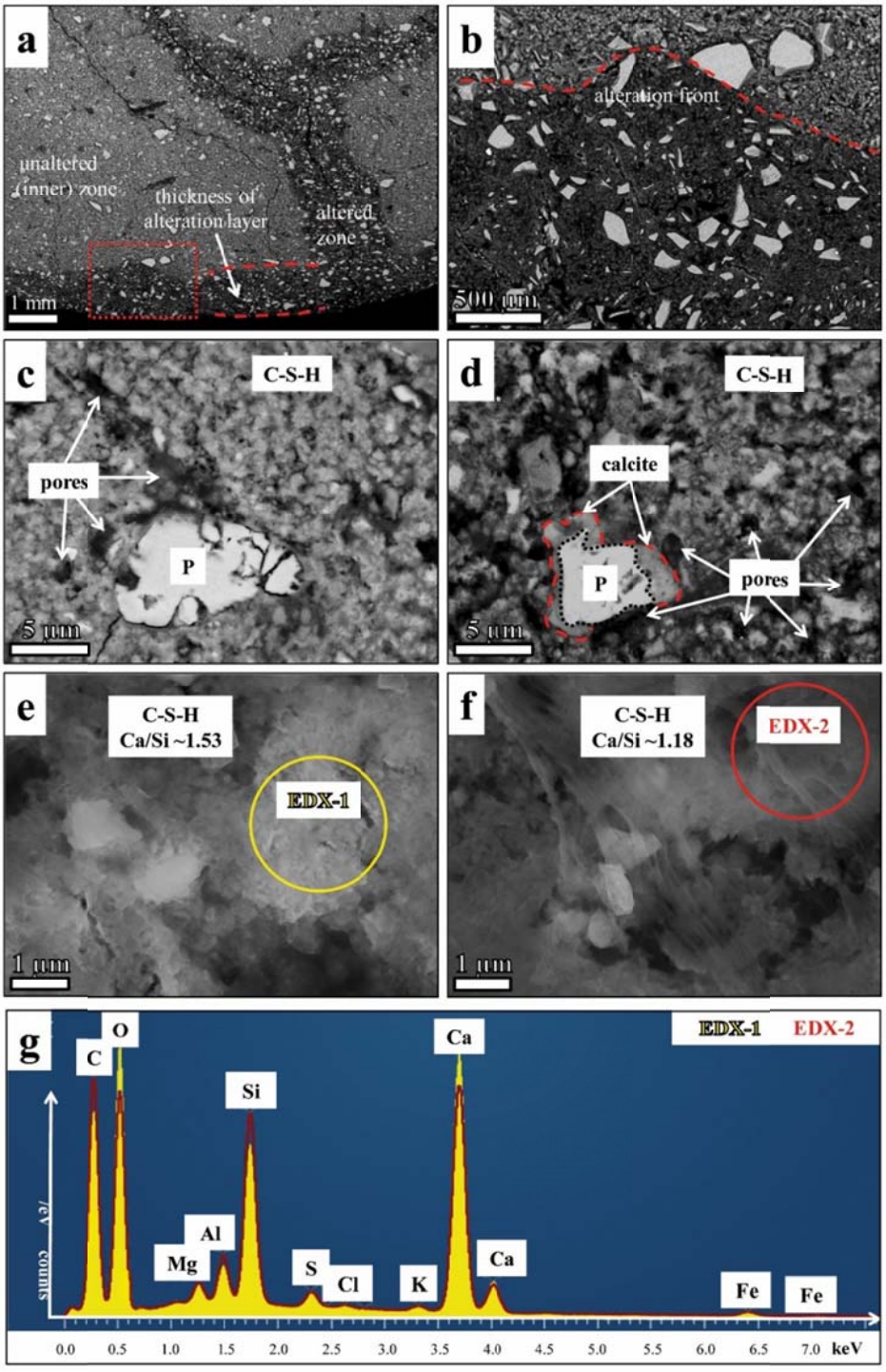

455

456 **Fig. 6.** (a) BSE image showing the transition zone between altered (dark grey areas with porous microfabrics)
457 and unaltered parts (light grey areas with denser microfabrics) of CEM_{100}. (b) Close-up of (a) marked with red
458 rectangle. Note the increase in porosity due to curing in weakly aggressive environments. (c,d) Close-ups
459 showing portlandite grains with/without thin calcite layers. (e,f) High-resolution BSE images displaying changes
460 in the particle form and Ca/Si molar ratio of C-S-H due to Ca-leaching and re-crystallization (e: inner zone; f:
461 outer zone). (g) Normalized EDX spectra of C-S-H from the unaltered (EDX-1) versus altered (EDX-2) zone
462 (spot positions are marked in e,f). P – portlandite.

463 *3.5.2 Thickness of leached layer*

464 The alteration front that developed around all types of hydrated cement blends was ~3.5 up to
465 ~12.3 times smaller compared to CEM_{100} after 182 days of reaction time (Table 3). In detail,
466 CEM_{30}/GS_{70}, CEM_{90}/SF_{10} and $CEM_{60}/MEF_{32.5}/MK_{7.5}$ displayed the smallest thicknesses of
467 the altered layer (< 0.2 mm), suggesting an outstanding resistance of these mixes against
468 calcium leaching and carbonation, judged by direct comparison with CEM_{100}. CEM_{90}/MK_{10}
469 and $CEM_{60}/MEF_{32.5}/MIF_{7.5}$ revealed alteration thicknesses of circa 0.4 mm, which justifies the
470 excellent performance of these mixes. Noteworthy, the alteration patterns observed were not
471 restricted immediately to the sample surface, as dissolution veins progressed into the deeper
472 parts (up to a few millimeters, Fig. 6a) of CEM_{100} (and $CEM_{60}/MEF_{32.5}/MK_{7.5}$). We therefore
473 conclude that exposure of cementitious materials to low-mineralized solutions undersaturated
474 with respect to the atmospheric CO_2 concentration can cause deterioration of the cement paste
475 within short times. This leaching process reduces the resistivity of steel-reinforced concrete to
476 carbonation, especially when subjected to wetting-drying cycles and under permanent
477 exposure to air.

478

479 *3.5.3 Microfabrics, C-S-H composition and porosity development*

480 Important microstructural data of the hydrated cement blends are provided in Table 3 for the
481 unaltered and altered zones of each sample. Corresponding BSE images are presented in
482 Figures 7 and 8. Note that all images have been collected at the same magnification and
483 brightness/contrast to ensure direct comparison between the samples.

484 In the unaltered zone, all cement pastes are dense, as indicated by total porosities from 5.7 ±
485 2.0 % to 9.5 ± 2.0 % (Table 3). The substitution of CEM 1 by SCMs decreased the portion of
486 clinker in the mixes and hence the water/clinker ratio (e.g. 40 % in $CEM_{60}/MEF_{32.5}/MIF_{7.5}$).
487 Nevertheless, the porosity in the unaltered zone was lower for all blended cements than for
488 CEM_{100}, up to 30 %. This is because of an increase in the total volume of the reaction

products that form in the cement blends upon cement hydration plus latent-hydraulic or pozzolanic reaction, compared to CEM_{100}. Indeed, the hydration of the cement blends with hydraulically active SCMs benefited from prolonged curing (182 days) at high water content (as defined by the w/b-ratio) and humidity. Regarding blends with inert limestone powders ($CEM_{60}/MEF_{32.5}/MIF_{7.5}$ and $CEM_{60}/MEF_{32.5}/MK_{7.5}$), the increased packing density due to a microfiller effect [11, 77] caused low porosity despite high water/clinker-ratios. All effects have resulted in a densification of the microstructure of the hydrated cement blends, as it is seen in the development of more fine pores and less coarse capillary pores than in CEM_{100} (Fig. 8c). This effect is particularly relevant for mixes containing MIF/MEF limestones.

Table 3. Compilation of microstructural data for the unaltered and altered zones of hydrated cement blends (see Fig. 6-8 for direct comparison of microfabrics, porosity and C-S-H composition) after 182 days of curing. Note the larger thickness of the corrosive layer and the increase in porosity in CEM_{100}, compared to all other cement blends, as well as the decrease in the Ca/Si ratio and the increase in the Al/Si molar toward the corrosion zone.

Sample ID	Thickness of corrosive layer (µm)	Sample description	Porosity (%)	Number of BSE images analyzed	Microfabric of C-S-H	Ca/Si ratio of C-S-H (molar)	Al/Si ratio of C-S-H (molar)	Number of EDX analyses
CEM_{100}	1470 ± 220	unaltered	9.5 ± 2 %	10	fine, dense	1.71 ± 0.20	0.12 ± 0.05	5
CEM_{100}		altered	23.2 ± 7 %	10	fibrillar, weak	1.23 ± 0.21	0.24 ± 0.09	6
CEM_{30}/GS_{70}	120 ± 40	unaltered	5.7 ± 2 %	9	foil-like, dense	1.39 ± 0.33	0.37 ± 0.04	6
CEM_{30}/GS_{70}		altered	6.2 ± 1 %	9	foil-like, dense	1.16 ± 0.27	0.32 ± 0.06	4
CEM_{90}/SF_{10}	170 ± 50	unaltered	6.9 ± 2 %	10	fine, dense	1.57 ± 0.14	0.14 ± 0.07	3
CEM_{90}/SF_{10}		altered	9.8 ± 2 %	8	fibrillar, weak	1.21 ± 0.09	0.25 ± 0.08	6
CEM_{90}/MK_{10}	370 ± 80	unaltered	6.4 ± 1 %	8	fine, dense	1.59 ± 0.22	0.31 ± 0.05	3
CEM_{90}/MK_{10}		altered	5.6 ± 12 %	10	foil-like, dense	1.32 ± 0.17	0.35 ± 0.06	5
$CEM_{60}/MEF_{32.5}/MIF_{7.5}$	420 ± 60	unaltered	7.3 ± 2 %	8	fine, dense	1.53 ± 0.25	0.16 ± 0.04	4
$CEM_{60}/MEF_{32.5}/MIF_{7.5}$		altered	8.0 ± 5 %	8	fine, dense	1.34 ± 0.11	0.23 ± 0.08	6
$CEM_{60}/MEF_{32.5}/MK_{7.5}$	210 ± 40	unaltered	6.2 ± 2 %	8	fine, dense	1.56 ± 0.19	0.27 ± 0.11	3
$CEM_{60}/MEF_{32.5}/MK_{7.5}$		altered	6.2 ± 3 %	8	foil-like, dense	1.32 ± 0.16	0.30 ± 0.07	5

C-S-H had a very fine or cloudy (Fig. 7a,e and Fig. 8a,c,e) to foil-like particle form (Fig. 7c). As expected, the chemical composition of C-S-H changed as a function of type and level of cement replacement by SCMs (Table 3), confirming predicted trends within the $CaO–Al_2O_3–SiO_2$ ternary diagram of cementitious materials [12]. This is seen by shifts in the molar ratios

507 of Ca/Si (1.71 ± 0.20 to 1.39 ± 0.33) and Al/Si (0.12 ± 0.05 to 0.37± 0.04) for CEM_{100} and
508 CEM_{30}/GS_{70}, respectively. M-A-S-H eventually formed in hydrated cements blended with
509 GS, MK, MEF and MIF, taking the high MgO contents (up to 3.5 wt-%) in the unaltered
510 samples and high hydrotalcite contents in the reacted samples (Fig. 3).

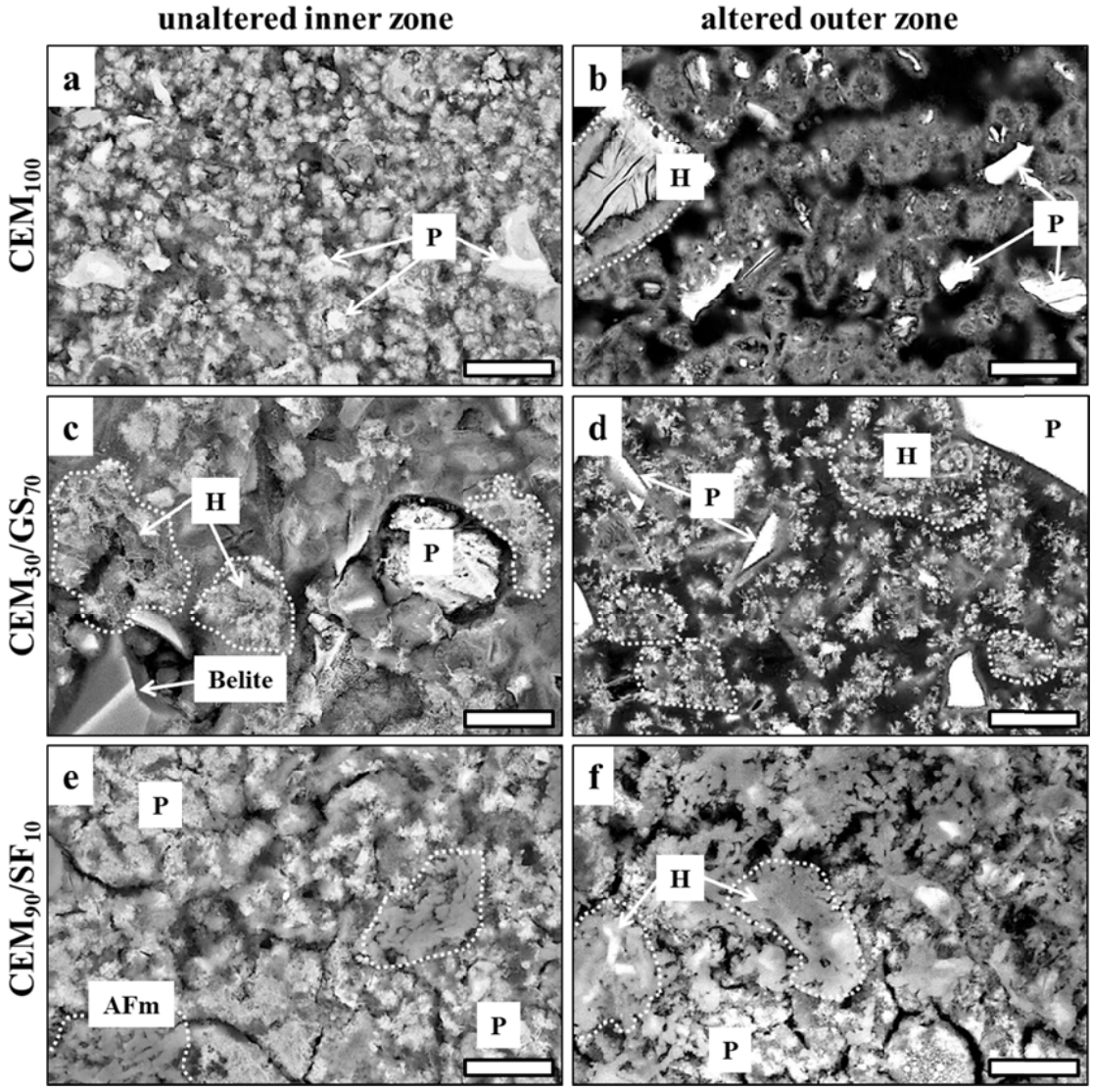

511

512 **Fig. 7.** BSE images showing the effect of SCM substitution for cement on the microfabrics of hydrated cement
513 blends and hydrated reference cement (i.e. inner zone) as well as alteration features associated with combined
514 calcium leaching and carbonation (i.e. altered outer zone). Microfabrics are denser and portlandite crystals are
515 smaller in hydrated cement blends, suggesting consumption of $Ca(OH)_2$ during hydration of SCMs. Note the
516 increase in porosity (especially in CEM_{100}), the formation of patches of hydrotalcite and the decrease in
517 brightness (i.e. reflecting a higher degree of calcium leaching from C--H, see Table 3) in the altered samples.
518 AFm –calcium aluminate hydrate, H – hydrotalcite, P – portlandite. Scale bar: 10 µm.

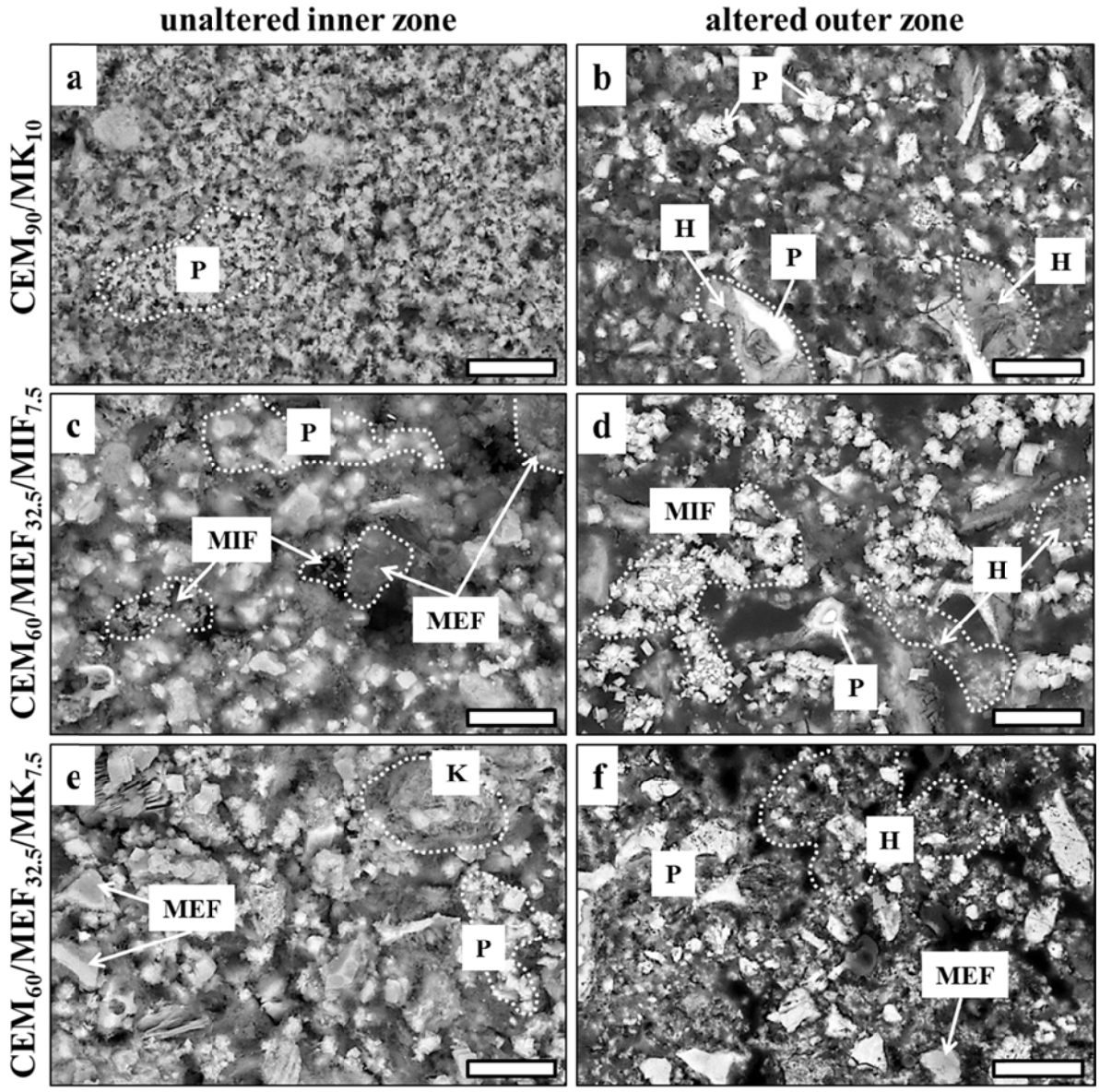

Fig. 8. Continuation of Fig. 7 showing the effect of SCM substitution for cement on the microfabrics of hydrated cement blends as well as alteration features due to curing in weakly aggressive environments. H – hydrotalcite, K – katoite, MEF – limestone mesofiller, MIF – limestone microfiller, P – portlandite. Scale bar: 10 μm.

The microstructure seen within the altered zone was completely different, compared to the unaltered zone (Table 3). For example, the microfabric was generally more porous (see Fig. 7b,f and Fig. 8f), as it is seen by a doubling in the total porosity of CEM_{100} and a moderate (~5-10 %) to high (~30 %) increase in the total porosities of all the other mixes, due both to portlandite dissolution and recrystallization of C-S-H. Abundant micro-cracks of variable thickness and length have been developed in this altered zone (see Fig. 6a for CEM_{100}). The

portlandite crystals, remaining after leaching, displayed a thin calcite layer (Fig. 7b,d and Fig. 8b,d) that prevented this phase from complete dissolution [22].

Microstructural modifications within the altered zones further included changes in the form of C-S-H particles (Table 3), altering from very fine and dense frameworks to fibrillary, foil-like and generally weaker ones (compare Fig. 7a,b and Fig. 8e,f). Moreover, recrystallized C-S-H had a lower Ca/Si molar ratio and a higher Al/Si molar ratio than the unaltered C-S-H (Table 3) due to leaching [16]. Taking this all together, significant deterioration of the microstructure of CEM_{100} relative to hydrated cement blends occurred over the course of leaching and carbonation, which expresses in a chemical weakening of the cement matrix and lack of cohesion between the cement paste and particles.

3.6 Comparison of leaching behavior of hydrated cement blends

The results of mineralogical, microstructural and geochemical changes of the hydrated cement blends due to leaching and carbonation attack can be summarized as follows: (i) a leached layer and pervasive cracks of variable thickness and length developed around the specimen`s surface, (ii) portlandite transformed into calcite (± vaterite) and very often a thin passivation layer of calcite formed around the portlandite crystals, (iii) tobermorite and katoite (± AFm phases) altered into hydrotalcite, (iv) the Ca/Si molar ratio of C-S-H decreased, while the Al/Si molar ratio increased within the alteration zone, and (v) the total porosity increased towards the active leaching and carbonation front.

Judging from these criteria, CEM_{100} preformed worse than the hydrated cement blends, since the reference mix exhibited the highest total porosity (Fig. 7 and 8), the highest portlandite loss (Fig. 5) and the highest decrease in the Ca/Si molar ratio of C-S-H (Fig. 6g and Table 3) among all the other samples under evaluation. This indicates that the decalcification process in OPC paste is generally faster than in the hydrated cement blends (Table 1). This is contrary to the results reported in Słomka-Słupik et al. [20], who have argued that slag-blended

555 materials degrade faster than CEM I during ammonium chloride attack, which they attributed
556 to the presence of micro-cracks along the slag grains and the high self-healing capacity of
557 OPC pastes. Such a self-healing effect, i.e. precipitation of secondary portlandite, was not
558 observed in this study, because the pore solutions were predominantly undersaturated with
559 respect to this mineral phase at any time of reaction (see Fig. 2f and Table S1). Consequently,
560 portlandite was consumed in favor of calcite precipitation, following reaction 1a-e:

561 $Ca(OH)_{2(s)} \leftrightarrow Ca^{2+} + 2OH^-$ (1a)

562 $CO_{2(g)} \leftrightarrow CO_{2(aq)}$ (1b)

563 $CO_{2(aq)} + OH^- \leftrightarrow HCO_3^-$ (1c)

564 $HCO_3^- \leftrightarrow CO_3^{2-} + H^+$ (1d)

565 $Ca^{2+} + CO_3^{2-} \leftrightarrow CaCO_{3(s)}$ (1e)

566 Ruiz-Agudo et al. [80] have proposed that no secondary porosity is generated during the
567 carbonation of portlandite. The data obtained in this study do not support this viewpoint, as it
568 can be inferred from the formation of micro-cracks, the increase in secondary porosity and the
569 expansion of the leaching front in CEM_{100} (Fig. 6a-d), i.e. the mix with the highest portlandite
570 loss. Progressive calcium leaching from the cement paste is evident by the disappearance of
571 tobermorite and katoite in the alteration zone (Fig. 3 and 4), and by the alteration of jennite-
572 type C-S-H to tobermorite-type C-S-H (Fig. 6 and Table 3), following to Eq. 2-6:

573 $Ca_5Si_6O_{16}(OH)_2 \cdot 7H_2O + 3H^+ \leftrightarrow 5Ca^{2+} + 6H_3SiO_4^- + OH^-$ (2)

574 $Ca_3Al_2(SiO_4)_{0.8}(OH)_{8.8} + 2.4H_2O \leftrightarrow 3Ca^{2+} + 2Al(OH)_4^- + 0.8H_3SiO_4^- + 3.2OH^-$ (3)

575 $M\text{-}S\text{-}H \leftrightarrow Mg^{2+} + H_3SiO_4^- + nH_2O$ (4)

576 $(CaO)_{1.67}(SiO_2)(H_2O)_{2.1} + 0.56H_2O \leftrightarrow 1.67Ca^{2+} + H_3SiO_4^- + 2.33OH^-$ (5)

577 $0.83Ca^{2+} + H_3SiO_4^- + 0.67OH^- \leftrightarrow (CaO)_{0.83}(SiO_2)(H_2O)_{1.33} + 0.51H_2O$ (6)

578 It is clear that these dissolution processes (Eq. 3-6) will produce secondary pore space within
579 the cement paste. Calcium leaching from C-S-H and subsequent alteration into a Ca-depleted
580 form (Eq. 7) is well-known to affect the mechanical properties (i.e. reduction of strength) and
581 solubility (expressed by the logarithm of the solubility constant for a certain mineral, $\log K_{sp}$)
582 of the hardened cement paste [81]. In this line, Walker et al. [75] have reported on an increase
583 in the $\log K_{sp}$ values, from -13.08 to -10.33, for C-S-H having Ca/Si molar ratios of 1.65 and
584 1.15, respectively, which is similar to the compositions determined in this study (Table 3). In
585 other words, this shift in the Ca/Si composition is equivalent to an increase of nearly three
586 orders of magnitude in solubility constants for the two forms of C-S-H.
587 We therefore suggest that dissolution and recrystallization phenomena within the cement
588 paste greatly affect the life performance of hydrated cement blends in leaching environments.
589 Specifically, the increase in total porosity and the higher solubility of Ca-depleted and highly
590 defect C-S-H are prone to facilitate the invasion of fluids from the outer environment after
591 initial leaching attack, like Cl^--bearing groundwater. Such interaction can promote e.g.
592 electrochemical corrosion of steel-reinforced concrete [10,31]. Furthermore, leaching of the
593 cement paste, following Eq. 3-6, liberates alkali hydroxides, Ca^{2+}, Mg^{2+} and Al^{3+} ions, and
594 silicic acid into the pore solutions (see Table S1), which creates conditions suitable both for
595 carbonation of C-S-H and precipitation of hydrotalcite, according to Eq. 7 and 8:

596 $$\text{C-S-H} + x\text{CO}_{2(g)} + \text{H}_2\text{O} \rightarrow \text{CaCO}_3 + \text{SiO}_2 \cdot n\text{H}_2\text{O} \quad (7)$$

597 $$\text{Mg}_4\text{Al}_2(\text{OH})_{12}\text{CO}_3 \cdot 3\text{H}_2\text{O} \leftrightarrow 4\text{Mg}^{2+} + 2\text{Al(OH)}_4^- + \text{CO}_3^{2-} + 4\text{OH}^- + 3\text{H}_2\text{O} \quad (8)$$

598 Mittermayr et al. [19] have proposed that the transformation of C-S-H into calcite generates
599 additional pore space, which also contributes to the increase in the secondary porosity of the
600 hydrated cement blends and especially CEM_{100} (Table 3). The dissolution of portlandite alone
601 is unlikely to generate such high porosities. This means that C-S-H decomposition generates
602 pore space particularly in CEM_{30}/GS_{70}, CEM_{90}/SF_{10} and CEM_{100}, taken the TGA results (Fig.

603 5 and Table 2), while all other mixes performed better. The reasons for this need further
604 investigation, but it is reasonable that this process affects the performance of hydrated cement
605 blends in corrosion environments. In this light, the role of hydrotalcite should be revisited,
606 because its formation is well-known to cause microstructural damage to the cement paste [64–
607 66]. On the other hand, precipitation of hydrotalcite can help preventing from steel corrosion,
608 as this mineral phase has a high affinity to bind Cl^- ions [82]. Further tests utilizing analogous
609 materials in contact with concentrated chlorine solutions will shed light on this issue.
610 In essence, from the datasets obtained in this study we infer that the substitution of cement by
611 various SCMs (up to 70 wt-%) does not negatively affect the resistance of hydrated cement
612 blends against leaching and carbonation. We refer this behavior to the different mineralogy,
613 chemistries and microstructures developing in pure cement paste versus cement blends upon
614 hydration, where an initially high $Ca(OH)_2$ content in the cement paste maintained a high pH-
615 buffering capacity throughout (i.e. CEM_{100}). Substitution of hydraulically active SCMs for
616 cement slightly reduced the $Ca(OH)_2$ content originally present in the cement paste due to its
617 reaction with the SCMs to form C-S-H phases; however, strongly alkaline pore solutions (pH
618 > 13) still evolved in all blended systems, reducing the risk of corrosion in the long term. The
619 spatiotemporal evolution of the alteration minerals (hydrotalcite, calcite and tobermorite-type
620 C-S-H) that form upon leaching and carbonation, and their distribution in the cement paste,
621 take another key control on the material`s performance, i.e. either physically protecting or
622 chemically weakening the cement paste depending on the original mix design. Probably most
623 importantly, pure cement paste developed an open pore structure with a higher porosity,
624 which facilitated leaching and carbonation, compared to all blended systems that generally
625 displayed lower total porosities, denser matrices, an increased amount of chemically less
626 reactive hydration products (mainly C-S-H) and/or inert components (e.g. micro-filler effect
627 induced by MEF and MIF additives), making the latter mix designs less vulnerable for
628 combined leaching and carbonation attack.

4. Conclusions

The effects of leaching and carbonation on the mineralogical, microstructural and chemical composition of hydrated cements, produced from CEM I 52.5R, and blended with high levels (up to 70 wt-%) of SCMs, have been evaluated. The following conclusions are drawn:

(1) A sharp transitional contact zone developed between the intact inner part and the altered outer part of each mix due to leaching and carbonation front penetration. The thickness of the altered layer reflects the degree of alteration, which was highest in pure CEM I.

(2) Carbonation of cement clinker phases, portlandite and C-S-H resulted in the precipitation of pore-clogging $CaCO_3$ polymorphs, and in the development of a thin passivation layer of calcite around the leached portlandite grains. Highest $CaCO_3$ deposition was found in CEM I, but carbonation of C-S-H was most efficient in mixes containing GS and SF.

(3) Portlandite, tobermorite, katoite and AFm phases disappeared towards to active leaching zone, whereas $CaCO_3$ phases and hydrotalcite formed within the leached layer. The progress of these coupled dissolution/re-precipitation processes can be monitored by chemical analysis and hydrochemical modelling of expressed pore solutions.

(4) A strong increase in pore space as well as changes in the particle form and composition of C-S-H were recognized in the altered versus unaltered paste of each mix. CEM I showed by far the highest increase in secondary porosity and the highest decrease in the Ca/Si molar ratio of C-S-H among all hydrated cement blends tested.

(5) All hydrated cement blends performed equal or better than CEM I, also of those blends with high portion of inert fillers (MEF, MIF) of the powder, which demonstrates their at least equivalent performance in mild leaching environments. This behavior can be explained by a densification of the cement paste by reaction of $Ca(OH)_2$ with SCMs and by a microfiller effect, induced by optimization of the packing density of the substituents.

Acknowledgements

This work was financially supported by the NAWI Graz (Graz Advanced School of Science, GASS) and by the Austrian Research Promotion Agency (FFG, 864288). The authors would like to thank G. Brunnsteiner, D. Graf, R. Panik (all from IMBT-TVFA, TU Graz) and S. Mertschnigg (FELMI-ZFE, TU Graz) for assistance during sample production and sample preparation. The support by the lab team of the IAG (TU Graz) during preparation of samples for mineralogical, thermogravimetric, spectroscopic and chemical analyses is acknowledged. The paper benefited from the constructive comments of two anonymous reviewers.

References

[1] V.L.. Bonavetti, H.A.. Donza, G.. Menendez, O.A.. Gabrera, E.F. Irassar, Limestone filler cement in low w/c concrete rational use of energy, Cem. Concr. Res. 33 (2003) 865–871.

[2] M. Schneider, M. Romer, M. Tschudin, H. Bolio, Sustainable cement production—present and future, Cem. Concr. Res. 41 (2011) 642–650. doi:http://dx.doi.org/10.1016/j.cemconres.2011.03.019.

[3] T. Proske, S. Hainer, M. Rezvani, C.A. Graubner, Eco-friendly concretes with reduced water and cement contents - Mix design principles and laboratory tests, Cem. Concr. Res. 51 (2013) 38–46. doi:10.1016/j.cemconres.2013.04.011.

[4] S. Palm, T. Proske, M. Rezvani, S. Hainer, C. Müller, C.A. Graubner, Cements with a high limestone content - Mechanical properties, durability and ecological characteristics of the concrete, Constr. Build. Mater. 119 (2016) 308–318. doi:10.1016/j.conbuildmat.2016.05.009.

[5] C. Shi, Z. Wu, J. Xiao, D. Wang, Z. Huang, Z. Fang, A review on ultra high performance concrete: Part I. Raw materials and mixture design, Constr. Build. Mater. 101 (2015) 741–751. doi:https://doi.org/10.1016/j.conbuildmat.2015.10.088.

[6] H.S. Müller, M. Haist, M. Vogel, Assessment of the sustainability potential of concrete and concrete structures considering their environmental impact, performance and lifetime, Constr. Build. Mater. 67 (2014) 321–337. doi:10.1016/j.conbuildmat.2014.01.039.

[7] T. Proske, S. Hainer, M. Rezvani, C.-A. Graubner, Eco-friendly concretes with reduced water and cement content – Mix design principles and application in practice, Constr. Build. Mater. 67 (2014) 413–421. doi:10.1016/j.conbuildmat.2013.12.066.

[8] E. Gartner, H. Hirao, A review of alternative approaches to the reduction of CO2emissions associated with the manufacture of the binder phase in concrete, Cem. Concr. Res. 78 (2015) 126–142. doi:10.1016/j.cemconres.2015.04.012.

[9] J. Carette, S. Staquet, Monitoring and modelling the early age and hardening behaviour of eco-concrete through continuous non-destructive measurements: Part II. Mechanical behaviour, Cem. Concr. Compos. 73 (2016) 1–9. doi:https://doi.org/10.1016/j.cemconcomp.2016.07.003.

[10] A. Scott, M.G. Alexander, Effect of supplementary cementitious materials (binder type) on the pore solution chemistry and the corrosion of steel in alkaline environments, Cem. Concr. Res. 89 (2016) 45–55. doi:10.1016/j.cemconres.2016.08.007.

[11] J. Juhart, G.A. David, C. Nickel, G. Fischer, F. Mittermayr, A new combined filler concept for eco-concrete, in: Proc. 14th Int. Congr. Chem. Cem. (ICCC 2015), Beijing, 2015.

[12] B. Lothenbach, K. Scrivener, R.D. Hooton, Supplementary cementitious materials, Cem. Concr. Res. 41 (2011) 1244–1256. doi:10.1016/j.cemconres.2010.12.001.

[13] M. Antoni, J. Rossen, F. Martirena, K. Scrivener, Cement substitution by a combination of metakaolin and limestone, Cem. Concr. Res. 42 (2012) 1579–1589. doi:https://doi.org/10.1016/j.cemconres.2012.09.006.

[14] E. Aprianti S, A huge number of artificial waste material can be supplementary cementitious material (SCM) for concrete production – a review part II, J. Clean. Prod. 142, Part (2017) 4178–4194. doi:https://doi.org/10.1016/j.jclepro.2015.12.115.

[15] F. Mittermayr, M. Rezvani, A. Baldermann, S. Hainer, P. Breitenbücher, J. Juhart, C.A. Graubner, T. Proske, Sulfate resistance of cement-reduced eco-friendly concretes, Cem. Concr. Compos. 55 (2015) 364–373. doi:10.1016/j.cemconcomp.2014.09.020.

[16] A. Baldermann, M. Rezvani, T. Proske, C. Grengg, F. Steindl, M. Sakoparnig, C. Baldermann, I. Galan, F. Emmerich, F. Mittermayr, Effect of very high limestone content and quality on the sulfate resistance of blended cements, Constr. Build. Mater. 188 (2018) 1065–1076. doi:10.1016/j.conbuildmat.2018.08.169.

[17] M. Romer, L. Holzer, M. Pfiffner, Swiss tunnel structures: concrete damage by formation of thaumasite, Cem. Concr. Compos. 25 (2003) 1111–1117. http://www.sciencedirect.com/science/article/B6TWF-49KH0ST-1/2/fe8f87b8d6ecb8541efc38c8294de399.

[18] S.T.. Lee, R.D.. Hooton, H.S.. Jung, D.H.. Park, C.S. Choi, Effect of limestone filler on the deterioration of mortars and pastes exposed to sulfate solutions at ambien temperature, Cem. Concr. Res. 38 (2008) 68–76.

[19] F. Mittermayr, A. Baldermann, C. Baldermann, G.H. Grathoff, D. Klammer, S.J. Köhler, A. Leis, L.N. Warr, M. Dietzel, Environmental controls and reaction pathways of coupled de-dolomitization and thaumasite formation, Cem. Concr. Res. 95 (2017) 282–293. doi:https://doi.org/10.1016/j.cemconres.2017.02.011.

[20] B. Słomka-Słupik, J. Podwórny, M. Staszuk, Corrosion of cement pastes made of CEM I and CEM III/A caused by a saturated water solution of ammonium chloride after 4 and 25 days of aggressive immersion, Constr. Build. Mater. 170 (2018) 279–289. doi:https://doi.org/10.1016/j.conbuildmat.2018.03.073.

[21] E.J. Garboczi, Microstructure and transport properties of concrete, in: J. Kropp, H.. Hilsdorf (Eds.), Rilem Rep. 12 – Perform. Criteria Concr. Durab. State Art Rep. by Rilem Tech. Comm. TC 116-PCD. Perform. Concr. as a Criterion Its Durab., E&FN Spon, 1995: pp. 198–212.

[22] I. Galan, A. Baldermann, W. Kusterle, M. Dietzel, F. Mittermayr, Durability of shotcrete for underground support– Review and update, Constr. Build. Mater. 202 (2019) 465–493. doi:10.1016/j.conbuildmat.2018.12.151.

[23] P. Blanc, X. Bourbon, A. Lassin, E.C. Gaucher, Chemical model for cement-based materials: Thermodynamic data assessment for phases other than C–S–H, Cem. Concr. Res. 40 (2010) 1360–1374.

729 doi:10.1016/j.cemconres.2010.04.003.
730 [24] N.C.M. Marty, O. Bildstein, P. Blanc, F. Claret, B. Cochepin, E.C. Gaucher, D. Jacques, J.-E. Lartigue,
731 S. Liu, K.U. Mayer, J.C.L. Meeussen, I. Munier, I. Pointeau, D. Su, C.I. Steefel, Benchmarks for
732 multicomponent reactive transport across a cement/clay interface, Comput. Geosci. 19 (2015) 635–653.
733 doi:10.1007/s10596-014-9463-6.
734 [25] H.F.W. Taylor, Cement Chemistry, Thomas Telford, 1997.
735 https://books.google.at/books?id=1BOETtwi7mMC.
736 [26] T. Matschei, B. Lothenbach, F.P. Glasser, The role of calcium carbonate in cement hydration, Cem.
737 Concr. Res. 37 (2007) 551–558. doi:http://dx.doi.org/10.1016/j.cemconres.2006.10.013.
738 [27] J. Stark, Recent advances in the field of cement hydration and microstructure analysis, Cem. Concr. Res.
739 41 (2011) 666–678. doi:http://dx.doi.org/10.1016/j.cemconres.2011.03.028.
740 [28] P. Feng, C. Miao, J.W. Bullard, A model of phase stability, microstructure and properties during
741 leaching of portland cement binders, Cem. Concr. Compos. 49 (2014) 9–19.
742 doi:https://doi.org/10.1016/j.cemconcomp.2014.01.006.
743 [29] Y. Ouyang, X. Chen, C. Lu, J. Fang, Properties of steel fiber and macro-synthetic fiber reinforced
744 shotcrete, Dongnan Daxue Xuebao (Ziran Kexue Ban)/Journal Southeast Univ. (Natural Sci. Ed.). 40
745 (2010) 44–48.
746 [30] V.B. Duong, R. Sahamitmongkol, S. Tangtermsirikul, Effect of leaching on carbonation resistance and
747 steel corrosion of cement-based materials, Constr. Build. Mater. 40 (2013) 1066–1075.
748 doi:10.1016/j.conbuildmat.2012.11.042.
749 [31] P. Choi, K.-K. Yun, J.H. Yeon, Effects of mineral admixtures and steel fiber on rheology, strength, and
750 chloride ion penetration resistance characteristics of wet-mix shotcrete mixtures containing crushed
751 aggregates, Constr. Build. Mater. 142 (2017) 376–384. doi:10.1016/j.conbuildmat.2017.03.093.
752 [32] R. Boch, M. Dietzel, P. Reichl, A. Leis, A. Baldermann, F. Mittermayr, P. Pölt, Rapid ikaite
753 ($CaCO3 \cdot 6H2O$) crystallization in a man-made river bed: Hydrogeochemical monitoring of a rarely
754 documented mineral formation, Appl. Geochemistry. 63 (2015) 366–379.
755 doi:10.1016/j.apgeochem.2015.10.003.
756 [33] J. Cowie, F.P. Glasser, The reaction between cement and natural waters containing dissolved carbon
757 dioxide, Adv. Cem. Res. 4 (1992) 119–134. doi:10.1680/adcr.1992.4.15.119.
758 [34] H.J. Wierig, Long-time studies on the carbonation of concrete under normal outdoor exposure, in: Rilem
759 Semin., Rilem Seminar on Durability of Concrete Structures under NOrmal Outdoor Exposure,
760 Hannover, n.d.
761 [35] D.E. Macphee, H.T. Cao, Theoretical description of impact of blast furnace slag (BFS) on steel
762 passivation in concrete, Mag. Concr. Res. 45 (1993) 63–69. doi:10.1680/macr.1993.45.162.63.
763 [36] B.G. Salvoldi, H. Beushausen, M.G. Alexander, Oxygen permeability of concrete and its relation to
764 carbonation, Constr. Build. Mater. 85 (2015) 30–37. doi:10.1016/j.conbuildmat.2015.02.019.
765 [37] A. Leemann, P. Nygaard, J. Kaufmann, R. Loser, Relation between carbonation resistance, mix design
766 and exposure of mortar and concrete, Cem. Concr. Compos. 62 (2015) 33–43.
767 doi:10.1016/j.cemconcomp.2015.04.020.
768 [38] F.P. Glasser, J. Marchand, E. Samson, Durability of concrete — Degradation phenomena involving
769 detrimental chemical reactions, Cem. Concr. Res. 38 (2008) 226–246.

770 http://www.sciencedirect.com/science/article/pii/S0008884607002190.
771 [39] B. Bary, Simplified coupled chemo-mechanical modeling of cement pastes behavior subjected to
772 combined leaching and external sulfate attack, Int. J. Numer. Anal. Methods Geomech. 32 (2008) 1791–
773 1816. doi:10.1002/nag.696.
774 [40] J. Wang, D. Niu, R. Ma, Y. Zhang, Investigation of sulfate attack resistance of shotcrete under dry-wet
775 cycles, J. Wuhan Univ. Technol. Sci. Ed. 31 (2016) 1329–1335. doi:10.1007/s11595-016-1535-0.
776 [41] M. Maslehuddin, M. Ibrahim, M. Shameem, M.R. Ali, M.H. Al-Mehthel, Effect of curing methods on
777 shrinkage and corrosion resistance of concrete, Constr. Build. Mater. 41 (2013) 634–641.
778 doi:10.1016/j.conbuildmat.2012.12.064.
779 [42] E. Güneyisi, T. Özturan, M. Gesoğlu, A study on reinforcement corrosion and related properties of plain
780 and blended cement concretes under different curing conditions, Cem. Concr. Compos. 27 (2005) 449–
781 461. doi:10.1016/j.cemconcomp.2004.05.006.
782 [43] EN 197-1, Cement - Part 1: Composition, specifications and conformity criteria for common cements,
783 (2011).
784 [44] A.S. El-Dieb, T.A. El-Maaddawy, Assessment of reinforcement corrosion protection of self-curing
785 concrete, J. Build. Eng. 20 (2018) 72–80. doi:10.1016/j.jobe.2018.07.007.
786 [45] J.H. Kim, S.W. Choi, K.M. Lee, Y.C. Choi, Influence of internal curing on the pore size distribution of
787 high strength concrete, Constr. Build. Mater. 192 (2018) 50–57. doi:10.1016/j.conbuildmat.2018.10.130.
788 [46] J. Tritthart, Chloride binding in cement II. The influence of the hydroxide concentration in the pore
789 solution of hardened cement paste on chloride binding, Cem. Concr. Res. 19 (1989) 683–691.
790 doi:10.1016/0008-8846(89)90039-2.
791 [47] F. Mittermayr, A. Baldermann, C. Kurta, T. Rinder, D. Klammer, A. Leis, J. Tritthart, M. Dietzel,
792 Evaporation — a key mechanism for the thaumasite form of sulfate attack, Cem. Concr. Res. 49 (2013)
793 55–64. doi:http://dx.doi.org/10.1016/j.cemconres.2013.03.003.
794 [48] S. Richoz, A. Baldermann, A. Frauwallner, M. Harzhauser, G. Daxner-Höck, D. Klammer, W.E. Piller,
795 Geochemistry and mineralogy of the Oligo-Miocene sediments of the Valley of Lakes, Mongolia,
796 Palaeobiodiversity and Palaeoenvironments. 97 (2017) 233–258. doi:10.1007/s12549-016-0268-6.
797 [49] A. Buades, B. Coll, J.-M. Morel, A Non-Local Algorithm for Image Denoising, in: 2005 IEEE Comput.
798 Soc. Conf. Comput. Vis. Pattern Recognit., IEEE, n.d.: pp. 60–65. doi:10.1109/CVPR.2005.38.
799 [50] P. Soille, Morphological Image Analysis, 2nd ed., Springer Berlin Heidelberg, Berlin, Heidelberg, 2004.
800 doi:10.1007/978-3-662-05088-0.
801 [51] A. Baldermann, A. Grießbacher, C. Baldermann, B. Purgstaller, I. Letofsky-Papst, S. Kaufhold, M.
802 Dietzel, Removal of Barium, Cobalt, Strontium, and Zinc from Solution by Natural and Synthetic
803 Allophane Adsorbents, Geosciences. 8 (2018) 309. doi:10.3390/geosciences8090309.
804 [52] D.L. Parkhurst, C.A.J. Appelo, User's guide to PHREEQC (V2), U.S. Geol. Sur. 312 (1999).
805 [53] B. Lothenbach, D.A. Kulik, T. Matschei, M. Balonis, L. Baquerizo, B. Dilnesa, G.D. Miron, R.J. Myers,
806 Cemdata18: A chemical thermodynamic database for hydrated Portland cements and alkali-activated
807 materials, Cem. Concr. Res. 115 (2019) 472–506. doi:https://doi.org/10.1016/j.cemconres.2018.04.018.
808 [54] L. Bertolini, B. Elsener, P. Pedeferri, R.B. Polder, Corrosion of Steel in Concrete: Prevention, Diagnosis,
809 Repair, Wiley-VCH Verlag GmbH & Co., Weinheim, 2005.
810 [55] Rasheeduzzafar, S.E. Hussain, A.S. Al-Gahtani, Pore solution composition and reinforcement corrosion

characteristics of microsilica blended cement concrete, Cem. Concr. Res. 21 (1991) 1035–1048. doi:https://doi.org/10.1016/0008-8846(91)90064-O.

[56] B. Purgstaller, M. Dietzel, A. Baldermann, V. Mavromatis, Control of temperature and aqueous Mg 2+ /Ca 2+ ratio on the (trans-)formation of ikaite, Geochim. Cosmochim. Acta. 217 (2017) 128–143. doi:10.1016/j.gca.2017.08.016.

[57] J.M. Rivas-Mercury, P. Pena, A.H. de Aza, X. Turrillas, Dehydration of Ca3Al2(SiO4)y(OH)4(3-y) (0 < y < 0.176) studied by neutron thermodiffractometry, J. Eur. Ceram. Soc. 28 (2008) 1737–1748. doi:10.1016/j.jeurceramsoc.2007.12.038.

[58] P.S. de Silva, F.P. Glasser, Phase relations in the system CaO□Al2O3□SiO2□H2O relevant to metakaolin - calcium hydroxide hydration, Cem. Concr. Res. 23 (1993) 627–639. doi:https://doi.org/10.1016/0008-8846(93)90014-Z.

[59] S.A. Bernal, J.L. Provis, B. Walkley, R.S. Nicolas, J.D. Gehman, D.G. Brice, A.R. Kilcullen, P. Duxson, J.S.J. van Deventer, Gel nanostructure in alkali-activated binders based on slag and fly ash, and effects of accelerated carbonation, Cem. Concr. Res. 53 (2013) 127–144. doi:https://doi.org/10.1016/j.cemconres.2013.06.007.

[60] T. Matschei, B. Lothenbach, F.P. Glasser, The AFm phase in Portland cement, Cem. Concr. Res. 37 (2007) 118–130. doi:10.1016/j.cemconres.2006.10.010.

[61] I.G. Richardson, Tobermorite/jennite- and tobermorite/calcium hydroxide-based models for the structure of C-S-H: applicability to hardened pastes of tricalcium silicate, β-dicalcium silicate, Portland cement, and blends of Portland cement with blast-furnace slag, metakaol, Cem. Concr. Res. 34 (2004) 1733–1777. doi:https://doi.org/10.1016/j.cemconres.2004.05.034.

[62] E. Bonaccorsi, S. Merlino, A.R. Kampf, The Crystal Structure of Tobermorite 14 A (Plombierite), a C-S-H Phase, J. Am. Ceram. Soc. 88 (2005) 505–512. doi:10.1111/j.1551-2916.2005.00116.x.

[63] S. Shaw, S.M. Clark, C.M.B. Henderson, Hydrothermal formation of the calcium silicate hydrates, tobermorite (Ca5Si6O16(OH)2·4H2O) and xonotlite (Ca6Si6O17(OH)2): an in situ synchrotron study, Chem. Geol. 167 (2000) 129–140. doi:https://doi.org/10.1016/S0009-2541(99)00205-3.

[64] I.G. Richardson, A.R. Brough, G.W. Groves, C.M. Dobson, The characterization of hardened alkali-activated blast-furnace slag pastes and the nature of the calcium silicate hydrate (C-S-H) phase, Cem. Concr. Res. 24 (1994) 813–829. doi:https://doi.org/10.1016/0008-8846(94)90002-7.

[65] M. Ben Haha, G. Le Saout, F. Winnefeld, B. Lothenbach, Influence of activator type on hydration kinetics, hydrate assemblage and microstructural development of alkali activated blast-furnace slags, Cem. Concr. Res. 41 (2011) 301–310. doi:https://doi.org/10.1016/j.cemconres.2010.11.016.

[66] R.J. Myers, S.A. Bernal, R. San Nicolas, J.L. Provis, Generalized structural description of calcium-sodium aluminosilicate hydrate gels: The cross-linked substituted tobermorite model, Langmuir. 29 (2013) 5294–5306. doi:10.1021/la4000473.

[67] S.N. Ghosh, A.K. Chatterjee, Absorption and reflection infra-red spectra of major cement minerals, clinkers and cements, J. Mater. Sci. 9 (1974) 1577–1584. doi:10.1007/BF00540754.

[68] S.N. Ghosh, S.K. Handoo, Infrared and Raman spectral studies in cement and concrete (review), Cem. Concr. Res. 10 (1980) 771–782. doi:10.1016/0008-8846(80)90005-8.

[69] M.D. Lane, P.R. Christensen, Thermal infrared emission spectroscopy of anhydrous carbonates, J. Geophys. Res. Planets. 102 (1997) 25581–25592. doi:10.1029/97JE02046.

852 [70] A. Baldermann, R. Dohrmann, S. Kaufhold, C. Nickel, I. Letofsky-Papst, M. Dietzel, The Fe-Mg-
853 saponite solid solution series – a hydrothermal synthesis study, Clay Miner. 49 (2014) 391–415.
854 doi:10.1180/claymin.2014.049.3.04.
855 [71] M. Horgnies, J.J. Chen, C. Bouillon, Overview about the use of fourier transform infrared spectroscopy
856 to study cementitious materials, WIT Trans. Eng. Sci. 77 (2013) 251–262. doi:10.2495/MC130221.
857 [72] E. Passaglia, R. Rinaldi, Katoite, a new member of the Ca3Al2(SiO4)3-Ca3Al2(OH)12 series and a new
858 nomenclature for the hydrogrossular group of minerals, Bull. Minéralogie. 107 (1984) 605–618.
859 doi:10.3406/bulmi.1984.7804.
860 [73] R. Żak, J. Deja, Spectroscopy study of Zn, Cd, Pb and Cr ions immobilization on C–S–H phase,
861 Spectrochim. Acta Part A Mol. Biomol. Spectrosc. 134 (2015) 614–620. doi:10.1016/j.saa.2014.06.069.
862 [74] P. Yu, R.J. Kirkpatrick, B. Poe, P.F. McMillan, X. Cong, Structure of Calcium Silicate Hydrate (C-S-H):
863 Near-, Mid-, and Far-Infrared Spectroscopy, J. Am. Ceram. Soc. 82 (2004) 742–748. doi:10.1111/j.1151-
864 2916.1999.tb01826.x.
865 [75] C.S. Walker, S. Sutou, C. Oda, M. Mihara, A. Honda, Calcium silicate hydrate (C-S-H) gel solubility
866 data and a discrete solid phase model at 25 °C based on two binary non-ideal solid solutions, Cem.
867 Concr. Res. 79 (2016) 1–30. doi:10.1016/j.cemconres.2015.07.006.
868 [76] Z. Pavlík, A. Trník, T. Kulovaná, L. Scheinherrová, V. Rahhal, E. Irassar, R. Černý, DSC and TG
869 Analysis of a Blended Binder Based on Waste Ceramic Powder and Portland Cement, Int. J.
870 Thermophys. 37 (2016) 1–14. doi:10.1007/s10765-016-2043-3.
871 [77] D. Wang, C. Shi, N. Farzadnia, Z. Shi, H. Jia, Z. Ou, A review on use of limestone powder in cement-
872 based materials: Mechanism, hydration and microstructures, Constr. Build. Mater. 181 (2018) 659–672.
873 doi:https://doi.org/10.1016/j.conbuildmat.2018.06.075.
874 [78] I. Garcia-Lodeiro, A. Palomo, A. Fernández-Jiménez, D.E. MacPhee, Compatibility studies between N-
875 A-S-H and C-A-S-H gels. Study in the ternary diagram Na2O-CaO-Al2O3-SiO 2-H2O, Cem. Concr.
876 Res. 41 (2011) 923–931. doi:10.1016/j.cemconres.2011.05.006.
877 [79] J.S.J. Van Deventer, J.L. Provis, P. Duxson, Technical and commercial progress in the adoption of
878 geopolymer cement, Miner. Eng. 29 (2012) 89–104. doi:10.1016/j.mineng.2011.09.009.
879 [80] E. Ruiz-Agudo, K. Kudłacz, C. V. Putnis, A. Putnis, C. Rodriguez-Navarro, Dissolution and carbonation
880 of portlandite [Ca(OH)2] single crystals, Environ. Sci. Technol. 47 (2013) 11342–11349.
881 doi:10.1021/es402061c.
882 [81] A. Baldermann, A. Landler, F. Mittermayr, I. Letofsky-Papst, F. Steindl, I. Galan, M. Dietzel, Removal
883 of heavy metals (Co, Cr, and Zn) during calcium–aluminium–silicate–hydrate and trioctahedral smectite
884 formation, J. Mater. Sci. (2019). doi:10.1007/s10853-019-03541-5.
885 [82] O. Kayali, M.S.H. Khan, M. Sharfuddin Ahmed, The role of hydrotalcite in chloride binding and
886 corrosion protection in concretes with ground granulated blast furnace slag, Cem. Concr. Compos. 34
887 (2012) 936–945. doi:10.1016/j.cemconcomp.2012.04.009.
888

889 # Electronic Appendix

890

891 **Table S1.** Chemical compositions of pore solutions of cement blends. Ion charge balance errors are < 3 %. SI –
892 saturation index, Cal – calcite, Jen – jennite, Tb – 14 Å-tobermorite, Ett – ettringite, Msa – monosulfoaluminate,
893 Mca/Hca – (mono/hemi)carboaluminate, Hgr – hydrogarnet, Htc – hydrotalcite, Por – portlandite.

Sample ID	**Exposure** days	**pH** -	**Na** mg/l	**K** mg/l	**Mg** mg/l	**Ca** mg/l	**Al** mg/l	**Si** mg/l	**OH** mg/l	**Cl** mg/l	**SO_4** mg/l	**CO_3** mg/l
CEM_{100}	28	13.5	3533	10948	2	20	16	56	6700	157	613	50
CEM_{100}	56	13.5	3534	11104	1	59	13	31	6749	169	464	47
CEM_{100}	91	13.5	3553	11142	6	83	19	10	6781	175	501	52
CEM_{100}	182	13.5	3971	12361	7	69	11	132	7216	230	751	47
CEM_{30}/GS_{70}	28	13.1	1375	4264	1	21	16	33	2723	52	94	41
CEM_{30}/GS_{70}	56	13.1	1325	4129	1	50	7	30	2417	110	159	44
CEM_{30}/GS_{70}	91	13.1	1385	4169	7	53	13	21	2667	64	118	48
CEM_{30}/GS_{70}	182	13.2	1712	5198	9	76	21	147	2800	86	206	45
CEM_{90}/SF_{10}	28	13.1	1579	4343	1	28	14	46	2640	195	353	40
CEM_{90}/SF_{10}	56	13.0	1367	3533	1	68	3	28	2167	238	165	43
CEM_{90}/SF_{10}	91	13.1	1434	3594	6	51	50	23	2349	173	271	37
CEM_{90}/SF_{10}	182	13.2	2343	5885	10	88	11	116	2041	313	289	42
CEM_{90}/MK_{10}	28	13.3	2159	5946	1	28	27	46	4053	55	115	35
CEM_{90}/MK_{10}	56	13.3	2198	5907	1	23	40	44	3909	62	139	43
CEM_{90}/MK_{10}	91	13.2	2122	5623	8	92	48	27	4004	75	82	38
CEM_{90}/MK_{10}	182	13.2	2042	5377	4	29	70	36	3745	74	130	40
$CEM_{60}/MEF_{32.5}/MIF_{7.5}$	28	13.3	2268	5985	2	179	9	31	4112	157	78	49
$CEM_{60}/MEF_{32.5}/MIF_{7.5}$	56	13.3	2218	5867	2	160	9	33	4100	203	98	54
$CEM_{60}/MEF_{32.5}/MIF_{7.5}$	91	13.3	2145	5859	8	175	2	19	3962	149	93	59
$CEM_{60}/MEF_{32.5}/MIF_{7.5}$	182	13.3	2443	6760	4	75	8	19	3808	244	197	51
$CEM_{60}/MEF_{32.5}/MK_{7.5}$	28	13.1	1572	3831	6	55	6	10	2584	47	28	47
$CEM_{60}/MEF_{32.5}/MK_{7.5}$	56	13.1	1638	3876	6	97	9	13	2738	70	51	55
$CEM_{60}/MEF_{32.5}/MK_{7.5}$	91	13.3	2127	6120	9	57	7	27	4521	135	132	56
$CEM_{60}/MEF_{32.5}/MK_{7.5}$	182	13.1	1812	4388	4	53	18	17	2663	126	110	50

894

895 **Table S1** Continued.

Sample ID	**Exposure** days	**SI_{Cal}** -	**SI_{Jen}** -	**SI_{Tb}** -	**SI_{Ett}** -	**SI_{Mca}** -	**SI_{Hca}** -	**SI_{Msa}** -	**SI_{Hgr}** -	**SI_{Htc}** -	**SI_{Por}** -
CEM_{100}	28	0.1	0.3	-0.3	-0.4	0.5	-0.5	-0.9	4.6	12.6	-0.5
CEM_{100}	56	0.6	0.8	-0.2	2.5	2.5	1.6	1.1	5.7	11.5	0.1
CEM_{100}	91	0.8	0.6	-1.3	4.1	3.7	2.7	2.2	6.2	15.2	0.3
CEM_{100}	182	0.4	1.3	1.1	2.2	2.0	1.1	0.7	5.8	14.1	0.0
CEM_{30}/GS_{70}	28	0.4	0.0	-0.2	-1.9	0.3	-1.1	-1.8	4.4	11.5	-0.9
CEM_{30}/GS_{70}	56	0.9	0.5	0.2	0.7	1.3	-0.1	-0.6	4.7	11.0	-0.5
CEM_{30}/GS_{70}	91	1.0	0.4	-0.3	1.2	2.2	0.7	0.1	5.3	15.2	-0.4
CEM_{30}/GS_{70}	182	0.7	1.1	1.6	1.5	2.1	0.8	0.3	6.1	14.7	-0.5
CEM_{90}/SF_{10}	28	0.5	0.3	0.3	0.2	0.5	-0.9	-1.0	4.6	11.1	-0.8
CEM_{90}/SF_{10}	56	1.1	0.6	0.3	0.9	1.1	-0.4	-0.7	4.3	10.3	-0.4

CEM_{90}/SF_{10}	91	0.9	0.3	-0.1	3.3	3.0	1.6	1.5	6.4	15.9	-0.5
CEM_{90}/SF_{10}	182	0.8	1.3	1.4	2.2	2.2	1.0	0.6	5.9	14.7	-0.2
CEM_{90}/MK_{10}	28	0.3	0.4	0.1	-0.7	1.2	0.1	-0.7	5.3	11.7	-0.6
CEM_{90}/MK_{10}	56	0.3	0.2	-0.1	-0.7	1.3	0.1	-0.6	5.4	12.1	-0.7
CEM_{90}/MK_{10}	91	1.0	0.9	0.0	3.2	4.3	3.1	2.2	7.2	16.4	0.0
CEM_{90}/MK_{10}	182	0.4	0.3	-0.1	0.6	2.3	1.1	0.4	6.2	15.2	-0.6
$CEM_{60}/MEF_{32.5}/MIF_{7.5}$	28	1.3	1.3	0.3	3.4	4.1	2.9	1.9	6.6	12.6	0.4
$CEM_{60}/MEF_{32.5}/MIF_{7.5}$	56	1.3	1.2	0.4	3.3	3.9	2.7	1.8	6.5	12.6	0.3
$CEM_{60}/MEF_{32.5}/MIF_{7.5}$	91	1.4	1.0	-0.2	2.3	2.9	1.7	0.7	5.1	13.9	0.3
$CEM_{60}/MEF_{32.5}/MIF_{7.5}$	182	0.9	0.7	-0.4	2.1	2.5	1.4	0.7	5.4	13.7	0.0
$CEM_{60}/MEF_{32.5}/MK_{7.5}$	28	1.0	0.1	-1.0	-1.0	1.7	0.3	-1.0	4.5	14.4	-0.4
$CEM_{60}/MEF_{32.5}/MK_{7.5}$	56	1.3	0.5	-0.6	1.6	3.1	1.7	0.6	5.6	14.8	-0.1
$CEM_{60}/MEF_{32.5}/MK_{7.5}$	91	0.9	0.6	-0.2	0.7	1.9	0.6	-0.2	5.0	15.0	-0.2
$CEM_{60}/MEF_{32.5}/MK_{7.5}$	182	0.9	0.3	-0.5	2.9	2.4	1.1	0.9	5.5	14.5	-0.4

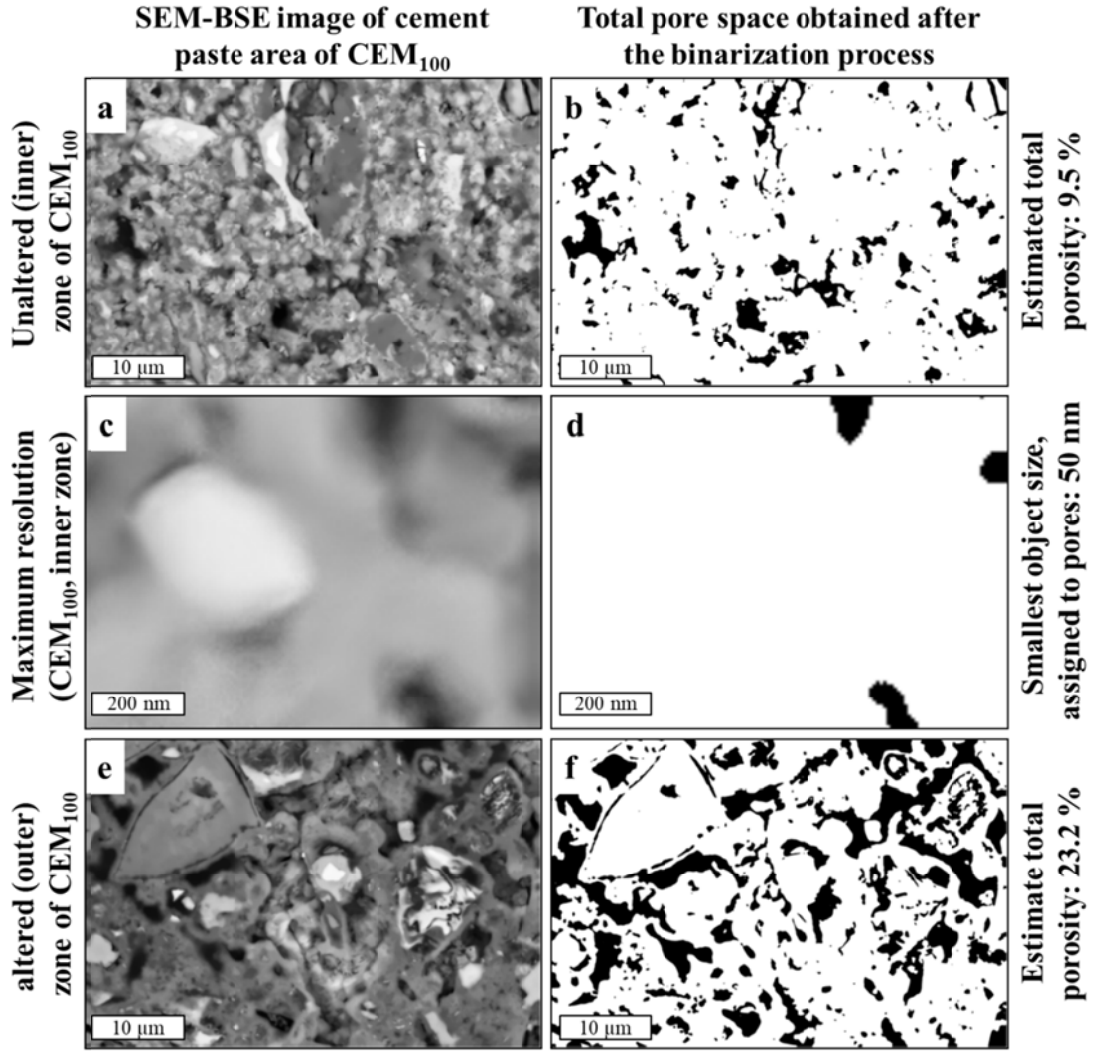

Fig. S1: Binarization process used to quantify the total porosity in the altered and unaltered zones of each mix design, with CEM_{100} as example.